GPU-ACCELERATED MONTE CARLO SIMULATION OF MV-CBCT

A Dissertation Presented

by

Mengying Shi

Submitted to the College of Science,

University of Massachusetts Lowell,

in partial fulfillment of the requirements for the degree of

DOCTOR OF PHILOSOPHY

May 2020

Medical Physics Program

ProQuest Number: 27832721

ProQuest

ProQuest 27832721

www.manaraa.com

GPU-ACCELERATED MONTE CARLO SIMULATION OF MV-CBCT

BY

MENGYING SHI
B.S. SHANGHAI JIAOTONG UNIVERSITY (2009)
M.S. SHANGHAI JIAOTONG UNIVERSITY (2011)
M.S. UNIVERSITY OF HEIDELBERG (2012)

SUBMITTED IN PARTIAL FULFILLMENT OF THE REQUIREMENTS FOR THE
DEGREE OF DOCTOR OF PHILOSOPHY
PHYSICS/MEDICAL PHYSICS OPTION
UNIVERSITY OF MASSACHUSETTS LOWELL

Signature of Author: **Date:**

Signature of Dissertation Co-Chair:
        Ross I. Berbeco, Ph.D.

Signature of Dissertation Co-Chair:
        Erno Sajo, Ph.D.

Signature of Other Dissertation Committee Members

Committee Member Signature:
        Wilfred Ngwa, Ph.D.

GPU-ACCELERATED MONTE CARLO SIMULATION OF MV-CBCT

BY
MENGYING SHI

ABSTRACT OF A DISSERTATION SUBMITTED TO THE FACULTY OF THE
DEPARTMENT OF PHYSICS AND APPLIED PHYSICS
IN PARRTIAL FULFILLMENT OF THE REQUIREMENTS

FOR THE DEGREE OF DOCTOR OF PHILOSOPHY
PHYSICS/MEDICAL PHYSICS OPTION
UNIVERSITY OF MASSACHUSETTS LOWELL
May 2020

Dissertation Supervisors:

Ross I. Berbeco, Ph.D.
Associate Professor, Department of Radiation Oncology
Brigham and Women's Hospital, Dana-Farber Cancer Institute, Harvard Medical School
Affiliate Faulty, Department of Physics and Applied Physics
University of Massachusetts Lowell

Erno Sajo, Ph.D.
Professor and Director, Medical Physics Program,
Department of Physics and Applied Physics
University of Massachusetts Lowell

ABSTRACT

High quality, low-dose mega-voltage cone-beam computed tomography (MV-CBCT) is important for image-guided radiation therapy and adaptive radiation therapy applications. It has advantages such as reduction of metal artifacts and limited effect of scatter radiation compared to kilo-voltage CBCT. Hence, it is desired to develop a novel MV imager for low-dose MV-CBCT. Digital prototyping of novel imager designs and simulating corresponding MV-CBCT results using Monte Carlo (MC) simulation avoid hardware implementation cost. However, the high computational complexity and prohibitively long execution time of MC simulation limits its use in imager design and other applications. In order to tackle this problem, a rapid, accurate simulation strategy for MV-CBCT accelerated by graphic processing unit is proposed and demonstrated in this research study.

We first developed a MC model of a MV imager, electronic portal-imaging device (EPID), and studied the impact of phosphor optical properties on the imager performance. The EPID model was built with a commonly used simulation software, GATE (Geant4 Application for Tomographic Emission). Radiative transport and optical transport were included in the imager model. Detective quantum efficiency (DQE), modulation transfer function (MTF), and normalized noise-power spectrum times the incident photon fluence (qNNPS) were computed and compared between the measured and simulated data. MTF was computed using the Fujita method. QNNPS was estimated using the Fujita-Lubberts-Swank (FLS) method. DQE was calculated from MTF and qNNPS. The agreement between measurement and simulation was good. The impact of five major optical

properties, on MTF, qNNPS, and DQE was demonstrated. The impact on MTF was less than that on qNNPS, while DQE(0) depends only on the phosphor thickness.

Based on the validated imager model, a novel method for rapid simulation of EPID planar image, FastEPID, was developed. The proposed method determines the detection of an incident photon using pre-calculated photon energy deposition and replaces imager response with precalculated OSFs. The FastEPID simulated images were compared with the experimentally acquired and conventionally simulated images in terms of MTF, signal-to-noise ratio (SNR), contrast-to-noise ratio (CNR), contrast, and relative difference of pixel value obtained with a contrast phantom and an anthropomorphic phantom. Great agreement between simulations and measurement was observed. The FastEPID method reduces the simulation time by factors of 90-140 without degrading the image quality.

By utilizing the FastEPID technique, we were able to quickly simulate phantom projections at different angles while maintaining the projection image accuracy. MV-CBCT images reconstructed from the FastEPID simulated projections were validated against the measured data in terms of cupping artifact, accuracy of Hounsfield unit (HU), CNR, and image noise. Projections of a Catphan 604 phantom and an anthropomorphic pelvis phantom were obtained under beam energies of 2.5 MV, 6 MV, and 6 MV flattening filter free (FFF). The agreement between measurement and FastEPID simulation was satisfactory. The proposed MV-CBCT simulation strategy was capable of reducing the run time performed on a CPU cluster to a matter of hours, rather than days or months required by a conventional MC simulation.

To further accelerate phantom simulation and bring the simulation work into a clinical-friendly environment, we presented a novel strategy for MV-CBCT simulation using graphic processing units (GPU). This strategy is designed in a way that generates a series of phantom projections from a single simulation run. Primary photons are generated from a beam source and saved properly in a particle batch. Since the beam source is independent from linear accelerator (Linac) gantry rotation, the same photon batch can be rotated and used repeatedly to simulate projections at different angles. A GPU-based Geant4 code is incorporated into the framework to simulate photon transport within the phantom volume. The FastEPID method is modified and integrated into the framework to generate projection images. Phantom projections at the same angle but generated from different batches are accumulated to form the final image. A standard Feldkamp-Davis Kress (FDK) algorithm is used for reconstruction with the projections extracted from the simulation. The proposed GPU-based simulation strategy was validated using the Catphan 604 phantom and the pelvis phantom with beam energies at 2.5 MV, 6 MV, and 6 MV FFF. The GPU-based simulation provided great accuracy and agreement with the measured and CPU-based simulated data. The MV-CBCT simulation time was shorted by a factor up to 2300 using an NVIDIA Tesla V100 GPU card against a 2.5 GHz AMD Opteron™ CPU Processor 6380.

ACKNOWLEDGEMENT

Mathias Lehmann, Pascal Huber, Paul Baturin, Rony Fueglistaller, and Daniel Morf, for their support and encouragement. It truly has been a great time working with you all.

I would like to acknowledge Massachusetts Green High Performance Computing Cluster for providing me with a vast amount of computational resources.

Furthermore, I want to thank my husband, Bo, and my parents, Lei and Shugui, for their unconditional love.

TABLE OF CONTENTS

LIST OF TABLES

LIST OF ILLUSTRATIONS

xiv

I.   INTRODUCTION

This chapter introduces the topic of my research study by reviewing the development of radiation therapy, image-guided radiation therapy (IGRT), mega-voltage (MV) imager, MV cone-beam computed tomography (MV-CBCT), Monte Carlo (MC) simulation, and graphics processing units (GPU). An overview of this research is provided at the end of the chapter.

1.1.   Radiation therapy

Radiation therapy is defined as a clinical modality using high-energy ionizing radiations for the treatment of cancer patients. The goal of radiation therapy is to deliver precious amounts of irradiation to tumor volume with minimized damage to surrounding normal tissues. Multiple radiation delivery systems are available for cancer treatment, such as external beam photon therapy, intro-operative radiation therapy, brachytherapy, proton therapy, and heavy charged particle therapy. For external beam photon therapy, the high-energy radiation is delivered to a carefully defined target volume in the forms of x-rays by a sophisticated linear accelerator. Subcategories of the external beam photon therapy include three-dimensional conformal radiation therapy (3DCRT), intensity-modulated radiation therapy (IMRT) with fixed gantry angles, IMRT with rotating fan beams (normally known as Tomotherapy), and volumetric modulated arc therapy (VMAT). Stereotactic radiosurgery (SRS) and stereotactic body radiation therapy (SBRT) are available for treatments of intracranial and extracranial tumors, respectively,

1

with unconventional dose fractionation (e.g. single fraction procedure in SRS and ultrahigh dose per fraction delivered in small amount of fractions in SBRT).

1.2.   Image-guided radiation therapy

Image-guided radiation therapy (IGRT) has been developed as a companion to beam-intensity modulation techniques, such as IMRT, VMAT, and SBRT, from an increased desire for a more accurate localization of tumor and normal issues. Multiple treatment stages can benefit from the guidance of imaging, especially pre-treatment patient setup, tumor localization, respiratory motion management, and real-time target tracking.

Various "in-room" imaging techniques are clinically available and have been integrated into the workflow of treatment to guide radiation delivery. On-board x-ray imaging (OBI) system is a pair of kilo-voltage (kV) x-ray tube and kV imager equipped on linear accelerator (Linac) gantry. The OBI system is mounted along an orthogonal orientation with respect to the treatment beam. It can be used to acquire high contrast planar radiographic image for visualization of bony landmarks and radio-opaque fiducials. The OBI system also has cone-beam computed tomography (kV-CBCT) capability by acquiring a series of patient projection images as the gantry rotates around the patient, from which three-dimensional (3D) volumetric images are reconstructed by using back-projection algorithm.

A MV imaging system, electronic portal imaging device (EPID), is mounted on the Linac gantry facing towards the treatment head. It is capable of acquiring patient planar images using the treatment beam for beam-eye view portal verification and real-time

2

target monitoring. The MV imaging system is also capable of MV-CBCT by acquiring patient projections from multiple directions as the gantry rotates, in a way similar to kV-CBCT.

Other modalities are also available for IGRT. A conventional diagnostic CT scanner housed in the treatment room acquires a high-resolution 3D volumetric data of patient anatomic structure, which can be used for pre-treatment positioning, dose calculation, and treatment re-planning. The scanner is normally installed on a sliding rail at the foot end of the treatment couch. The patient is rotated with the couch by 180° to align with the CT scanner for image acquisition. Ultrasound is a commonly used technique for real-time soft tissues and tumors localization. This noninvasive imaging modality does not introduce extra imaging dose to patient. However, the poor image quality and complexity of interpretation have hindered its broad use in radiation therapy. An alternative way to achieve good visualization of the soft tissue and tumors is to merge a magnetic resonance imaging device (MRI) and a Linac into a single machine called "MR-Linac". The MR portion allows an accurate localizing and monitoring of tumors while avoiding extra radiation dose to the patient. By combining a Linac with a positron emission tomography-CT (PET-CT), the accuracy of tumor localization can be improved significantly using the cancer cells attached with PET radiotracers as biological beacons. Management of respiratory motion relies on the real-time IGRT techniques including four-dimensional (4D) CT, fluoroscopy-based tracking system, electromagnetic field tracking system, and MRI-based volumetric tracking system.

3

1.3.   Mega-voltage (MV) imager and MV cone-beam computed tomography

1.3.1. Development of MV imager and EPID

The most commonly used clinical EPID consists of a metal build-up layer, a gadolinium oxysulfide (GOS) phosphor screen, and an amorphous silicon (a-Si) flat panel detector array. The phosphor screen consists of phosphor grains packed within a binder material. During image acquisition, energies of the incident x-ray photons are deposited in the GOS phosphor layer and optical photons are generated through scintillation interactions. The final EPID image is then generated from the detection of optical photons that enter the a-Si panel detector. This imager design can withstand a high radiation exposure and allows fast digital image acquisition (Antonuk, 2002; El-Mohri *et al.*, 1999; van Elmpt *et al.*, 2008; Blake *et al.*, 2013). The EPID detection efficiency of MV x-ray photons is roughly 1%-1.5%, which can be improved by a new imager design (El-Mohri *et al.*, 2001).

Various attempts were made to increase the EPID detection efficiency. As an alternative to phosphor films, segmented crystalline scintillators were capable of providing a high DQE (Mosleh-Shirazi *et al.*, 1998; Sawant *et al.*, 2005; Star-Lack *et al.*, 2015; Wang *et al.*, 2008). According to a study by Sawant *et al*., the DQE(0) of the segmented crystalline scintillator was approximately 22 times greater than that of a conventional active matrix flat panel imager. Also, Star-Lack *et al*. reported a DQE(0) more than 20 times higher than that of a conventional copper /phosphor imager design. A novel EPID based on a multi-layer structure was reported and provided roughly four-five times higher DQE(0) than that of a reference EPID (Myronakis *et al.*, 2017; Rottmann *et*

4

al., 2016). A fully detailed introduction of the multi-layer imager (MLI) can be found in Section 1.3.3.

1.3.2. MV cone-beam computed tomography

MV-CBCT has been developed for patient positioning and monitoring before and during treatment (Barker *et al.*, 2004). A series of patient projection images are acquired using EPID as Linac rotates around the patient, from which the MV-CBCT images are reconstructed. X-ray source of the MV-CBCT scan is the MV treatment beam.

The first clinical MV-CBCT system using 6 MV treatment beam was developed by a collaboration between University of California, San Francisco and Siemens (Siemens Medical Systems, Concord, CA) in 2001. Follow-up studies have reported the development and implementation of MV-CBCT. Pouliot *et al.* demonstrated that a low-dose MV-CBCT has sufficient image quality for image registration with a kV planning CT (Pouliot *et al.*, 2005). Aubin *et al*. presented the implementation of MV-CBCT for complementing the planning CT with the presence of metallic structures (Aubin *et al.*, 2006). Gayou *et al*. evaluated the impact of image acquisition protocols on the reconstructed MV-CBCT image quality (Gayou *et al.*, 2007). Other studies reported the implementation of MV-CBCT for dose calculation (Morin *et al.*, 2007b; Morin *et al.*, 2007a; Aubry *et al.*, 2008).

MV-CBCT can be used for dose reconstruction and treatment planning because the linear attenuation coefficients (μ) are reconstructed at the treatment beam's energy (Langen *et al.*, 2005). Other advantages of MV-CBCT includes metal artifacts reduction and limited effect of scatter radiation compared to kV-CBCT (Pouliot *et al.*, 2005; Yin *et al.*, 2005; Morin *et al.*, 2006). However, the image quality of MV-CBCT is not

5

satisfactory due to the low detection efficiency of the commonly used EPID (Antonuk, 2002; El-Mohri *et al.*, 2001). Because of these advantages and challenges, MV-CBCT has become a significant motivator for the development of new EPID designs (El-Mohri *et al.*, 2011; Hu *et al.*, 2018; Hu *et al.*, 2019; Myronakis *et al.*, 2018; Myronakis *et al.*, 2019; Wang *et al.*, 2008).

1.3.3. Multi-layer imager

The multi-layer imager (MLI) is a novel EPID developed for high quality and low-dose MV imaging. As shown in Figure **1**, the MLI consists of four identical and separated layers of copper build-up plate, phosphor, and panel detector array (Rottmann *et al.*, 2016). Output of the MLI can be a combined image from all layers or four images each exported from a single layer, depending on the imaging task. This detector provides a detective quantum efficiency (DQE) of 6.7% at zero frequency, which is approximately four times of DQE(0) of the most clinically used EPID, Varian AS1200 (Varian Medical System, Palo Alto, USA). Signal-to-noise ratio (SNR) of the all-layer-combined image increases by a factor of 1.7 compared to that of the single layer image. Modulation transfer function (MTF) of all-layer-combined and single layer agrees well indicating the spatial resolution is maintained with the stacked structure. Several clinical applications are expected to benefit from this MV imager design. Myronakis *et al.* reported the feasibility of low-dose MV-CBCT using the MLI (Myronakis *et al.*, 2020). Average Hounsfield unit (HU) uniformity of the reconstructions tested with a Catphan 604 phantom was in the range of 95%-99% for beam energies 2.5 MV, 6 MV, and 6 MV flattening filter free (FFF). Relative electron density of the phantom inserts estimated from the corresponding HU values agreed well with the nominal values with a negligible

6

difference of 0.4% ± 1.8%. Contrast-to-noise ratio of the phantom inserts increased by a factor of 2-4 compared to that acquired with AS1200 imager.
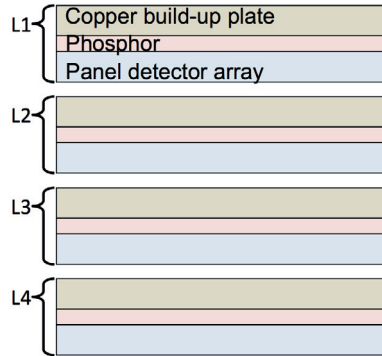
Figure 1 Cross-sectional view of the multi-layer imager.

1.4. Monte Carlo simulation

The Monte Carlo (MC) method is a computational technique that is normally used to solve physical and mathematical problems by randomly sampling appropriate probability distributions. It has been considered to be the most accurate computation approach for image formation (Ay *et al.*, 2004; Ay and Zaidi, 2005; Boone *et al.*, 2000; Myronakis *et al.*, 2017) and dose calculation (Paganetti *et al.*, 2008; Wang *et al.*, 1998). MC simulation has shown great clinical potential in treatment planning and optimization (Cygler *et al.*, 2004; Heath *et al.*, 2004; Herman *et al.*, 2001), dosimetry computation (Ma and Nahum, 1993; Ma *et al.*, 1993), and imager optimization (Shi *et al.*, 2018; Wang *et al.*, 2008). Multiple MC simulation packages have been developed and widely validated against measured data, and the available packages include Geant4 (Agostinelli *et al.*, 2003; Carrier *et al.*, 2004), MCNP (Brown *et al.*, 2002), EGSnrc (Kawrakow, 2000b, a), and PENELOPE (Baro *et al.*, 1995; Sempau *et al.*, 2001).

7

1.4.1. Monte Carlo simulation of EPID

In the literature, there has been a large number of studies using MC techniques to explore the physics interaction within the EPID model and to help optimize imager design in the absence of an expensive and time-consuming physical prototype.

An EGS4-based MC model for Varian AS500 was developed by Siebers *et al* (Siebers *et al.*, 2004)*.* A water layer was attached to the back of the imager to compensate for backscatters. Energy deposition in the phosphor layer was recorded using a virtual detector-scoring methodology to form the EPID image (Siebers *et al.*, 2004). Ko *et al* reported a MC model of AS500 imager to study the impact of different backscattering materials for the optimization of the backscatter effects (Ko *et al.*, 2004). A Geant4-based MC model for Varian AS1000 was built by Star-Lack *et al*. (Star-Lack *et al.*, 2014). To accurately and rapidly compute noise power spectrum (NPS) of the imager, a novel method, Fujita-Lubberts-Swank (FLS) method, was proposed, which requires only 10 to 100 x-ray photons detected per flood image. Excellent agreement was shown between the measured and calculated EPID performance. Myronakis *et al.* developed a simulation model for the multi-layer imager utilizing Geant4 application for tomographic emission (GATE) software. The model was validated against the experimentally acquired data such as MTF, NPS, and DQE. Good agreement between the measured and simulated data was demonstrated (Myronakis *et al.*, 2017).

Other MC studies have explored the impact of phosphor properties on EPID imaging performance. Radcliffe *et al.* reported the effect of the phosphor thickness and metal thickness on energy deposition, photon detection efficiency, and signal-to-noise ratio (Radcliffe *et al.*, 1993). The impact of the thickness and composition of

8

metal/phosphor screen on MTF, NPS, and DQE at MeV mono-energetic photon beams was evaluated by Kausch *et al*, showing a greater DQE for imagers with metal layer of high atomic number (Kausch *et al.*, 1999). In this study, the optical transport was computed as a convolution of energy deposition and optical spread function. Liaparinos *et al.* evaluated the impact of phosphor grain size and packing ratio on MTF and found that a small grain size and a high packing ratio would improve imager resolution (Liaparinos *et al.*, 2006). The dependence of the scattering transport parameters on the optical emission spectrum and grain size distribution has been investigated by Poludniowski and Evans utilizing two geometrical optic models (Poludniowski and Evans, 2013). High sensitivity of the scattering transport parameters on emission spectrum and grain size were reported. Photon absorption efficiency and MTF were simulated with each parameter value, but no evaluation of the imager NPS was computed. The impact of different optical transport parameters on the EPID dosimetric response was investigated by Blake *et al* (Blake *et al.*, 2013). This study demonstrated how the full width at tenth maximum (FWTM) and full width at half maximum (FWHM) of the point spread function (PSF) varied with each parameter value (Blake *et al.*, 2013). It has been shown that optical properties can impact the imager performance. For MV imaging, MTF and x-ray absorption are significant factors to consider. However, noise performance is equally important and should be estimated simultaneously.

In general, EPID optimization requires the developing and testing of various detector designs. By utilizing MC technique, this process can be significantly accelerated. Meanwhile, the hardware implementation costs can be avoided.

1.4.2. Drawback of current EPID simulation and potential solutions

The major drawback of EPID MC simulation is the long computation time attributed to tracking of a large number of primary photons, secondary electrons, and optical photons. Due to the low detector efficiency, EPID images are normally acquired at a relatively high image dose, which means more primary particles to track and longer time to compute during MC simulation. Further, a larger number of optical photons are generated by each scintillation event. Tracking those optical photons also requires long simulation time. Blake *et al.* reported that simulation of a single EPID image with 10^7 primary particles required approximately 3000 CPU-hours (Blake *et al.*, 2013). Also, roughly 7×10^5 CPU-hours required to simulate several MV-CBCT scans excluding optical photon transport was reported by Wang *et al.* (Wang *et al.*, 2008). Shi *et al.* reported 1.383×10^6 CPU-hours was required to simulated a Las Vegas phantom EPID image at 1 MU (Shi *et al.*, 2019).

Several attempts have been made to shorten the simulation time without degrading EPID simulation accuracy. A MC model of the Varian AS1000 EPID was built by Star-Lack *et al.*, and the scintillation yield of GOS phosphor was decreased from 60,000 photons/MeV to 400 photons/MeV, saving a significant amount of computational time (Star-Lack *et al.*, 2014). An AS1200 EPID was developed utilizing a scintillation yield of 600 photons/MeV (Shi *et al.*, 2018). No significant difference of MTF, NPS, and DQE between simulation and measured was observed. To avoid optical photon transport, an EPID image can be obtained by the convolution between the energy deposition of absorbed x-rays and the pre-defined optical blurring kernel (Kausch *et al.*, 1999; Kirkby and Sloboda, 2005). The methods described above are demonstrated to shorten the

10

simulation time by approximating optical transports, but still suffer from time-consuming simulation of radiation transport.

1.5.   Graphics processing unit (GPU) accelerated Monte Carlo simulation

Most of the MC simulation applications are limited by long execution time due to its stochastic nature. One potential solution is to run the simulation in a parallel fashion. Distributing identical jobs to a high performance computing cluster for simultaneous processing is such a solution, but it is not practical in a clinical environment due to limited number of available CPU cores, data storage capacity, and data transfer speeds. A more practical approach is to use graphics processing unit (GPU).

1.5.1. Introduction of GPU

GPUs are computation engines for intensive parallel processing. A GPU card normally contains millions of basic units, called "threads". The threads are organized in blocks and handled by multiple streaming processors. They process data with the same program code, called a kernel. GPUs have several memory spaces for data storage. Global memory is largest memory, generally up to several gigabytes (GB). Local memory and shared memory are smaller in size but have a quick access. CUDA is a computing application programming interface developed by NVIDIA (NVIDIA, Santa Clara, CA, USA). It is used for GPU programming and the execution of computation.

1.5.2. GPU-accelerated Monte Carlo simulation

MC simulation utilizing GPU has been introduced in radiation therapy. Multiple studies have demonstrated GPU simulation of photon transport (Badal and Badano, 2009; Fang and Boas, 2009; Jia et al., 2012b; Lo et al., 2009), coupled photon-electron

transport (Hissoiny *et al.*, 2011; Jahnke *et al.*, 2012; Jia *et al.*, 2011), and proton transport (Jia *et al.*, 2012a; Wan Chan Tseung *et al.*, 2015), all achieving significant reduction in computation time. Treatment plan optimization and dose calculation based on MC simulation have been successfully implemented on GPU, allowing a clinical application of MC simulations (Hissoiny *et al.*, 2011; Jahnke *et al.*, 2012; Jia *et al.*, 2011; Ma *et al.*, 2014; Men *et al.*, 2009; Men *et al.*, 2010).

However, there have been limited studies on the development of GPU-based imaging simulation. A Geant4-based GPU implementation for medical imaging applications was introduced by Bert *et al.* (Bert *et al.*, 2013). It performed the phantom simulation by translating the Geant4-based code from a CPU environment to a GPU environment. Image simulation was approximated by counting the number of detected particles assuming an ideal detector with 100% detection efficiency. A GPU tool, gDRR, for the simulation of kV-CBCT projections was developed and demonstrated by Jia *et al.* (Jia *et al.*, 2012b). The imager response of gDRR was simplified to be the energy deposition determined with the incident photon energy and a pre-defined response curve. Clinical EPID has low detection efficiency (1%-1.5%) and contains both radiative and optical physics processes for image acquisition (Antonuk, 2002). Neither the number of detected photons nor the photon energy deposition can provide an accurate estimation of the MV imager response. Therefore, an accurate approximation of the imager response needs to be considered for the GPU-based MC simulation of EPID image and MV-CBCT.

1.6.   This dissertation and the outline

In this work, we investigate the acceleration of EPID image simulation and MV-CBCT simulation. The aim is to propose a MC simulation framework that would generate a full set of MV-CBCT projections within hours. We believe both software and hardware improvements are key to the acceleration of MV-CBCT simulation.

Our research started with developing a MC computational model of the most commonly used EPID, Varian AS1200. Based on the validated imager model, we studied the impact of varying optical properties on imager performance and developed a novel computational algorithm, FastEPID, to speed up EPID image simulation. Implementation of the FastEPID method on MV-CBCT simulation was demonstrated by simulating a series of phantom projections on high performance computing CPU cluster. Finally, a novel MV-CBCT simulation framework utilizing FastEPID method and GPU cards was proposed.

Chapter 2 describes a MC model of Varian AS1200 and demonstrates the dependence of the imager performance on five major optical properties, phosphor grain size, phosphor thickness, phosphor refractive index, binder refractive index, and packing ratio.

Chapter 3 reports a novel method, FastEPID, for fast image simulation of EPID using pre-calculated imager responses. The proposed method determines the photon detection through a comparison between a random number and the pre-calculated photon energy deposition, and replaces EPID response with precalculated optical spread functions (OSF). Without degrading image quality, the FastEPID method can reduce simulation time by a factor up to 140.

13

Chapter 4 describes a rapid simulation strategy for MV-CBCT utilizing the FastEPID method. This novel strategy reduces the run time of a full scan simulation of MV-CBCT performed on a CPU cluster to a matter of hours while accurately reproducing the image qualities of the reconstruction.

Chapter 5 presents a novel simulation framework of MV-CBCT using a graphic processing unit (GPU). The proposed framework is capable of generating a series of phantom projections from a single simulation run. It demonstrates great simulation accuracy compared to measurement and CPU-based simulation in terms of reconstructed image qualities. The MV-CBCT simulation can be accelerated by factors of roughly 900 – 2300 by utilizing the proposed GPU-based simulation framework.

In chapter 6, the main conclusion of our research is summarized and recommendations for future study and clinical implementation are discussed.

1.7.   Reference

Agostinelli S, Allison J, Amako K a, Apostolakis J, Araujo H, Arce P, Asai M, Axen D, Banerjee S and Barrand G 2003 GEANT4—a simulation toolkit *Nuclear instruments and methods in physics research section A: Accelerators, Spectrometers, Detectors and Associated Equipment* **506** 250-303

Antonuk L E 2002 Electronic portal imaging devices: a review and historical perspective of contemporary technologies and research *Phys Med Biol* **47** R31-65

Aubin M, Morin O, Chen J, Gillis A, Pickett B, Aubry J F, Akazawa C, Speight J, Roach M, 3rd and Pouliot J 2006 The use of megavoltage cone-beam CT to complement CT for target definition in pelvic radiotherapy in the presence of hip replacement *Br J Radiol* **79** 918-21

Aubry J F, Pouliot J and Beaulieu L 2008 Correction of megavoltage cone-beam CT images for dose calculation in the head and neck region *Med Phys* **35** 900-7

Ay M R, Shahriari M, Sarkar S, Adib M and Zaidi H 2004 Monte carlo simulation of x-ray spectra in diagnostic radiology and mammography using MCNP4C *Phys Med Biol* **49** 4897-917

Ay M R and Zaidi H 2005 Development and validation of MCNP4C-based Monte Carlo simulator for fan- and cone-beam x-ray CT *Phys Med Biol* **50** 4863-85

14

Badal A and Badano A 2009 Accelerating Monte Carlo simulations of photon transport in a voxelized geometry using a massively parallel graphics processing unit *Med Phys* **36** 4878-80

Barker J L, Jr., Garden A S, Ang K K, O'Daniel J C, Wang H, Court L E, Morrison W H, Rosenthal D I, Chao K S, Tucker S L, Mohan R and Dong L 2004 Quantification of volumetric and geometric changes occurring during fractionated radiotherapy for head-and-neck cancer using an integrated CT/linear accelerator system *Int J Radiat Oncol Biol Phys* **59** 960-70

Baro J, Sempau J, Fernández-Varea J and Salvat F 1995 PENELOPE: an algorithm for Monte Carlo simulation of the penetration and energy loss of electrons and positrons in matter *Nuclear Instruments and Methods in Physics Research Section B: Beam Interactions with Materials and Atoms* **100** 31-46

Bert J, Perez-Ponce H, El Bitar Z, Jan S, Boursier Y, Vintache D, Bonissent A, Morel C, Brasse D and Visvikis D 2013 Geant4-based Monte Carlo simulations on GPU for medical applications *Phys Med Biol* **58** 5593-611

Blake S J, Vial P, Holloway L, Greer P B, McNamara A L and Kuncic Z 2013 Characterization of optical transport effects on EPID dosimetry using Geant4 *Med Phys* **40** 041708

Boone J M, Buonocore M H and Cooper V N, 3rd 2000 Monte Carlo validation in diagnostic radiological imaging *Med Phys* **27** 1294-304

Brown F B, Barrett R, Booth T, Bull J, Cox L, Forster R, Goorley T, Mosteller R, Post S and Prael R 2002 MCNP version 5 *Trans. Am. Nucl. Soc* **87** 02-3935

Carrier J F, Archambault L, Beaulieu L and Roy R 2004 Validation of GEANT4, an object-oriented Monte Carlo toolkit, for simulations in medical physics *Med Phys* **31** 484-92

Cygler J E, Daskalov G M, Chan G H and Ding G X 2004 Evaluation of the first commercial Monte Carlo dose calculation engine for electron beam treatment planning *Med Phys* **31** 142-53

El-Mohri Y, Antonuk L E, Yorkston J, Jee K W, Maolinbay M, Lam K L and Siewerdsen J H 1999 Relative dosimetry using active matrix flat-panel imager (AMFPI) technology *Med Phys* **26** 1530-41

El-Mohri Y, Antonuk L E, Zhao Q, Choroszucha R B, Jiang H and Liu L 2011 Low-dose megavoltage cone-beam CT imaging using thick, segmented scintillators *Physics in Medicine & Biology* **56** 1509

El-Mohri Y, Jee K W, Antonuk L E, Maolinbay M and Zhao Q 2001 Determination of the detective quantum efficiency of a prototype, megavoltage indirect detection, active matrix flat-panel imager *Med Phys* **28** 2538-50

Fang Q and Boas D A 2009 Monte Carlo simulation of photon migration in 3D turbid media accelerated by graphics processing units *Opt Express* **17** 20178-90

Gayou O, Parda D S, Johnson M and Miften M 2007 Patient dose and image quality from mega-voltage cone beam computed tomography imaging *Med Phys* **34** 499-506

Heath E, Seuntjens J and Sheikh-Bagheri D 2004 Dosimetric evaluation of the clinical implementation of the first commercial IMRT Monte Carlo treatment planning system at 6 MV *Med Phys* **31** 2771-9

15

Herman M G, Balter J M, Jaffray D A, McGee K P, Munro P, Shalev S, Van Herk M and Wong J W 2001 Clinical use of electronic portal imaging: report of AAPM Radiation Therapy Committee Task Group 58 *Medical Physics* **28** 712-37

Hissoiny S, Ozell B, Bouchard H and Despres P 2011 GPUMCD: A new GPU-oriented Monte Carlo dose calculation platform *Med Phys* **38** 754-64

Hu Y, Baturin P, Wang A, Rottmann J, Myronakis M, Fueglistaller R, Huber P, Shi M, Shedlock D and Morf D *MEDICAL PHYSICS,2018),* vol. Series 45*)*: WILEY 111 RIVER ST, HOBOKEN 07030-5774, NJ USA) pp E461-E

Hu Y H, Shedlock D, Wang A, Rottmann J, Baturin P, Myronakis M, Huber P, Fueglistaller R, Shi M and Morf D 2019 Characterizing a novel scintillating glass for application to megavoltage cone‐beam computed tomography *Medical physics* **46** 1323-30

Jahnke L, Fleckenstein J, Wenz F and Hesser J 2012 GMC: a GPU implementation of a Monte Carlo dose calculation based on Geant4 *Phys Med Biol* **57** 1217-29

Jia X, Gu X, Graves Y J, Folkerts M and Jiang S B 2011 GPU-based fast Monte Carlo simulation for radiotherapy dose calculation *Phys Med Biol* **56** 7017-31

Jia X, Schumann J, Paganetti H and Jiang S B 2012a GPU-based fast Monte Carlo dose calculation for proton therapy *Phys Med Biol* **57** 7783-97

Jia X, Yan H, Cervino L, Folkerts M and Jiang S B 2012b A GPU tool for efficient, accurate, and realistic simulation of cone beam CT projections *Med Phys* **39** 7368-78

Kausch C, Schreiber B, Kreuder F, Schmidt R and Dossel O 1999 Monte Carlo simulations of the imaging performance of metal plate/phosphor screens used in radiotherapy *Med Phys* **26** 2113-24

Kawrakow I 2000a Accurate condensed history Monte Carlo simulation of electron transport. I. EGSnrc, the new EGS4 version *Med Phys* **27** 485-98

Kawrakow I 2000b Accurate condensed history Monte Carlo simulation of electron transport. II. Application to ion chamber response simulations *Med Phys* **27** 499-513

Kirkby C and Sloboda R 2005 Comprehensive Monte Carlo calculation of the point spread function for a commercial a-Si EPID *Med Phys* **32** 1115-27

Ko L, Kim J O and Siebers J V 2004 Investigation of the optimal backscatter for an aSi electronic portal imaging device *Phys Med Biol* **49** 1723-38

Langen K M, Meeks S L, Poole D O, Wagner T H, Willoughby T R, Kupelian P A, Ruchala K J, Haimerl J and Olivera G H 2005 The use of megavoltage CT (MVCT) images for dose recomputations *Phys Med Biol* **50** 4259-76

Liaparinos P F, Kandarakis I S, Cavouras D A, Delis H B and Panayiotakis G S 2006 Modeling granular phosphor screens by Monte Carlo methods *Med Phys* **33** 4502-14

Lo W C, Redmond K, Luu J, Chow P, Rose J and Lilge L 2009 Hardware acceleration of a Monte Carlo simulation for photodynamic therapy [corrected] treatment planning *J Biomed Opt* **14** 014019

Ma C M and Nahum A E 1993 Calculation of absorbed dose ratios using correlated Monte Carlo sampling *Med Phys* **20** 1189-99

16

Ma C M, Rogers D W, Shortt K R, Ross C K, Nahum A E and Bielajew A F 1993 Wall-correction and absorbed-dose conversion factors for Fricke dosimetry: Monte Carlo calculations and measurements *Med Phys* **20** 283-92

Ma J, Beltran C, Seum Wan Chan Tseung H and Herman M G 2014 A GPU-accelerated and Monte Carlo-based intensity modulated proton therapy optimization system *Med Phys* **41** 121707

Men C, Gu X, Choi D, Majumdar A, Zheng Z, Mueller K and Jiang S B 2009 GPU-based ultrafast IMRT plan optimization *Phys Med Biol* **54** 6565-73

Men C, Romeijn H E, Jia X and Jiang S B 2010 Ultrafast treatment plan optimization for volumetric modulated arc therapy (VMAT) *Med Phys* **37** 5787-91

Morin O, Chen J, Aubin M, Gillis A, Aubry J F, Bose S, Chen H, Descovich M, Xia P and Pouliot J 2007a Dose calculation using megavoltage cone-beam CT *Int J Radiat Oncol Biol Phys* **67** 1201-10

Morin O, Gillis A, Chen J, Aubin M, Bucci M K, Roach M, 3rd and Pouliot J 2006 Megavoltage cone-beam CT: system description and clinical applications *Med Dosim* **31** 51-61

Morin O, Gillis A, Descovich M, Chen J, Aubin M, Aubry J F, Chen H, Gottschalk A R, Xia P and Pouliot J 2007b Patient dose considerations for routine megavoltage cone-beam CT imaging *Med Phys* **34** 1819-27

Mosleh-Shirazi M A, Swindell W and Evans P M 1998 Optimization of the scintillation detector in a combined 3D megavoltage CT scanner and portal imager *Med Phys* **25** 1880-90

Myronakis M, Huber P, Fueglistaller R, Wang A, Hu Y, Baturin P, Shi M, Morf D, Star-Lack J and Berbeco R *MEDICAL PHYSICS,2018), vol. Series 45)*: WILEY 111 RIVER ST, HOBOKEN 07030-5774, NJ USA) pp E461-E2

Myronakis M, Huber P, Lehmann M, Fueglistaller R, Jacobson M, Hu Y H, Baturin P, Wang A, Shi M, Harris T, Morf D and Berbeco R 2020 Low-dose megavoltage cone-beam computed tomography using a novel multi-layer imager (MLI) *Med Phys*

Myronakis M, Huber P, Lehmann M, Fueglistaller R, Jacobson M, Shi M, Ferguson D, Lozano I V, Baturin P and Harris T *MEDICAL PHYSICS,2019), vol. Series 46)*: WILEY 111 RIVER ST, HOBOKEN 07030-5774, NJ USA) pp E397-E

Myronakis M, Star-Lack J, Baturin P, Rottmann J, Morf D, Wang A, Hu Y H, Shedlock D and Berbeco R I 2017 A novel multilayer MV imager computational model for component optimization *Med Phys* **44** 4213-22

Paganetti H, Jiang H, Parodi K, Slopsema R and Engelsman M 2008 Clinical implementation of full Monte Carlo dose calculation in proton beam therapy *Phys Med Biol* **53** 4825-53

Poludniowski G G and Evans P M 2013 Optical photon transport in powdered-phosphor scintillators. Part II. Calculation of single-scattering transport parameters *Med Phys* **40** 041905

Pouliot J, Bani-Hashemi A, Chen J, Svatos M, Ghelmansarai F, Mitschke M, Aubin M, Xia P, Morin O, Bucci K, Roach M, 3rd, Hernandez P, Zheng Z, Hristov D and Verhey L 2005 Low-dose megavoltage cone-beam CT for radiation therapy *Int J Radiat Oncol Biol Phys* **61** 552-60

17

Radcliffe T, Barnea G, Wowk B, Rajapakshe R and Shalev S 1993 Monte Carlo optimization of metal/phosphor screens at megavoltage energies *Med Phys* **20** 1161-9

Rottmann J, Morf D, Fueglistaller R, Zentai G, Star-Lack J and Berbeco R 2016 A novel EPID design for enhanced contrast and detective quantum efficiency *Phys Med Biol* **61** 6297-306

Sawant A, Antonuk L E, El-Mohri Y, Zhao Q, Li Y, Su Z, Wang Y, Yamamoto J, Du H, Cunningham I, Klugerman M and Shah K 2005 Segmented crystalline scintillators: an initial investigation of high quantum efficiency detectors for megavoltage x-ray imaging *Med Phys* **32** 3067-83

Sempau J, Sanchez-Reyes A, Salvat F, ben Tahar H O, Jiang S B and Fernandez-Varea J M 2001 Monte Carlo simulation of electron beams from an accelerator head using PENELOPE *Phys Med Biol* **46** 1163-86

Shi M, Myronakis M, Hu Y H, Jacobson M, Lehmann M, Fueglistaller R, Huber P, Baturin P, Wang A, Ferguson D, Harris T, Morf D and Berbeco R 2019 A novel method for fast image simulation of flat panel detectors *Phys Med Biol* **64** 095019

Shi M, Myronakis M, Hu Y H, Morf D, Rottmann J and Berbeco R 2018 A Monte Carlo study of the impact of phosphor optical properties on EPID imaging performance *Phys Med Biol* **63** 165013

Siebers J V, Kim J O, Ko L, Keall P J and Mohan R 2004 Monte Carlo computation of dosimetric amorphous silicon electronic portal images *Med Phys* **31** 2135-46

Star-Lack J, Shedlock D, Swahn D, Humber D, Wang A, Hirsh H, Zentai G, Sawkey D, Kruger I, Sun M, Abel E, Virshup G, Shin M and Fahrig R 2015 A piecewise-focused high DQE detector for MV imaging *Med Phys* **42** 5084-99

Star-Lack J, Sun M, Meyer A, Morf D, Constantin D, Fahrig R and Abel E 2014 Rapid Monte Carlo simulation of detector DQE(f) *Med Phys* **41** 031916

van Elmpt W, McDermott L, Nijsten S, Wendling M, Lambin P and Mijnheer B 2008 A literature review of electronic portal imaging for radiotherapy dosimetry *Radiother Oncol* **88** 289-309

Wan Chan Tseung H, Ma J and Beltran C 2015 A fast GPU-based Monte Carlo simulation of proton transport with detailed modeling of nonelastic interactions *Med Phys* **42** 2967-78

Wang L, Chui C S and Lovelock M 1998 A patient-specific Monte Carlo dose-calculation method for photon beams *Med Phys* **25** 867-78

Wang Y, Antonuk L E, El-Mohri Y, Zhao Q, Sawant A and Du H 2008 Monte Carlo investigations of megavoltage cone-beam CT using thick, segmented scintillating detectors for soft tissue visualization *Med Phys* **35** 145-58

Yin F F, Guan H and Lu W 2005 A technique for on-board CT reconstruction using both kilovoltage and megavoltage beam projections for 3D treatment verification *Med Phys* **32** 2819-26

II. A MONTE CARLO STUDY OF VARIAN AS1200 IMAGER AND THE PHOSPHOR OPTICAL PROPERTIES

In this chapter, the first detailed Geant4-based MC computational model of Varian AS1200 was built and validated. The impact of five major optical properties on EPID image performance was evaluated. This chapter is based on published work: Shi M, Myronakis M, Hu Y H, Morf D, Rottmann J and Berbeco R. A MC study of the impact of phosphor optical properties on EPID imaging performance *Phys Med Biol* **63** 165013 (2018) (Shi *et al.*, 2018).

2.1. Materials and methods

2.1.1. AS1200 EPID structure

There are three major components of the AS1200 imager: a copper layer, a phosphor screen, and an a-Si panel detector (Antonuk, 2002). The copper layer converts incident photons into secondary electrons and shields low energy scattered radiations. The phosphor screen converts deposited energies into optical photons through scintillation processes. The a-Si panel detector detects the incident optical photons and generates EPID image. The phosphor screen is a Lanex Fast-Back screen (Carestream Health, Rochester, NY). It consists of a reflective support layer, a Gd2O2S:Tb (GOS) phosphor layer, and a protection layer. Surface density of the GOS phosphor layer is 133 mg/cm^2 and the mass density is 4.59 g/cm^3. The packing ratio, the ratio of phosphor grain volume to the total phosphor layer volume, is 62%. The a-Si panel detector can be

19

approximated to a silicon dioxide (SiO$_2$) slab in simulation. The detector pitch is 0.336 mm and the readout array has 1280 × 1280 pixels. Two alloy layers, Al and Pb, are attached to the back of the imager for backscatter shielding. The thickness and density of each layer is listed in Table **1**, and the model geometry is illustrated in Figure **2**.

Table 1 Physical properties of AS1200 imager.

Structure	Density	Thickness
Copper buildup	8.9 g/cm^3	1 mm
Reflective support	1.38 g/cm^3	0.18 mm
Phosphor (GOS)	4.59 g/cm^3	0.29 mm
Protection foil	1.38 g/cm^3	0.075 mm
a-Si Panel detector	2.6 g/cm^3	0.7 mm
Aluminum alloy	2.8 g/cm^3	1 mm
Lead alloy	10.95 g/cm^3	3 mm
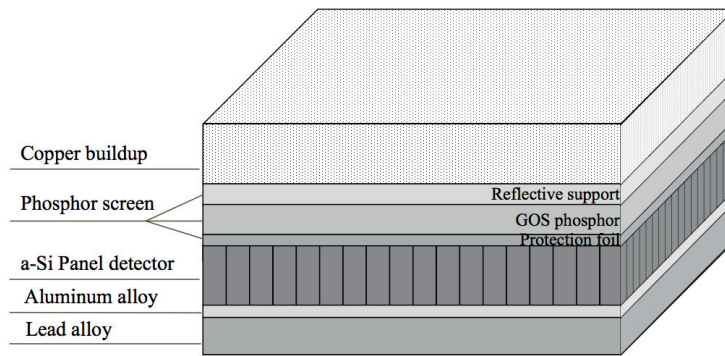
Figure 2 AS1200 model geometry (not to scale).

2.1.2. Physics models, beam model, and AS1200 model

A MC simulation software, GATE (Geant4 application for tomographic emission), was employed for imager modeling and simulation studies (Jan *et al.*, 2011; Sarrut *et al.*,

20

2014). GATE is capable of simulating transports of x-ray/gamma photons, optical photons, and charged particles (Agostinelli *et al.*, 2003; Allison *et al.*, 2006). It has been widely used for imaging and dosimetry purposes (Grevillot *et al.*, 2011; Maigne *et al.*, 2011). GATE v8.0 and Geant4 v10.03.p01 were used in this study. All simulations of this chapter were performed on a Linux system equipped with twelve 3.8 GHz CPU cores and 16 GB of RAM.

2.1.2.1. Radiative and optical physics model

Due to a satisfactory accuracy and acceptable computational speed, PENELOPE was chosen as the radiative physics list in this study (Star-Lack et al., 2014). The electromagnetic processes available for simulation included photoelectric effect, Compton scattering, pair production, Rayleigh scattering, ionization, bremsstrahlung, annihilation, etc. The range cut values for photons and electrons were set to 5 μm.

The optical processes available for simulation included scintillation, absorption, reflection and refraction at boundaries, and scattering. The GOS phosphor has a scintillation yield (SY) of approximately 60000 optical photons per MeV energy deposition (opticals/MeV). In this study, a lower SY (600 opticals/MeV) was used to reduce the computation time without reducing the simulation accuracy of optical response (Star-Lack et al., 2014).

The optical photon wavelength was set to 0.545 μm, which was the dominant wavelength in the emission spectrum of the GOS phosphor. Diameter of the phosphor grains was set to 7 μm (Poludniowski and Evans, 2013a). Refractive indices of the GOS grain and the phosphor binder were set to 2.3 and 1.0, respectively (Myronakis *et al.*,

21

2017). The absorption length of the GOS phosphor was set to 43 mm (Poludniowski and Evans, 2013a).

Both Rayleigh scattering and Mie scattering were enabled in this simulation. For EPID modeling, Mie scattering was the dominant optical interaction due to the large GOS grain size with respect to the optical photon wavelength (Myronakis *et al.*, 2017). The reflective support layer on top of the GOS phosphor was modeled as a white PET layer with 88% reflectivity at 545 nm. The detailed optical processes and the corresponding parameters are listed in Table **2**.

2.1.2.2.   Source beam model

The measured images were acquired at Linac 6 MV beam energy. During image simulation, energies of the primary photons were sampled from the corresponding 6 MV x-ray spectrum. This spectrum was extracted from Varian TrueBeam phase space files that are generated above the secondary collimators of Linac (Varian Medical System, Palo Alto, USA) (Constantin *et al.*, 2011). The phase space files are available for download on International Atomic Energy Agency website.

2.1.2.3.   AS1200 imager model

The AS1200 imager model consists of a number of uniform slabs representing the imager components as listed in Table **1**. Physical density and thickness of each layer were set in the model following the information described in Section 2.1.1. For simulation convenience, the imager was modeled with a readout array size of 446×446 pixels and a pitch of 0.336 mm, giving a detection area of 150×150 mm^2.

Table 2 Optical properties and reference values of AS1200 imager.

Structure	Parameter	AS1200
Reflective layer	PET reflectivity	88%
	Refractive index	1.58
	Absorption length	10 mm
GOS phosphor	Grain size	7 μm (diameter)
	Phosphor refractive index	2.3
	Scintillation yield	600 optical/MeV
	Absorption length	43 mm
	Mie scattering length	0.00346 mm
	Binder refractive index	1.0
	Photon emission wavelength	545 nm
Protection foil	Refractive index	1.58
	Absorption length	10 mm
Panel detector	Refractive index	1.52
	Absorption length	0.0001 mm

2.1.3. Measurement of MTF, qNNPS, and DQE

Three image quality metrics were computed for the validation and investigation of AS1200 performance: MTF, normalized NPS times incident x-ray fluence (qNNPS), and DQE. MTF describes the imager signal performance. QNNPS describes the imager noise transfer property. DQE describes the imager signal-to-noise performance (Siewerdsen *et al.*, 1998).

23

The AS1200 MTF was measured by using Fujita method with a slanted slit image (Fujita *et al.*, 1992). The slit image was acquired by illuminating the AS1200 imager with a narrow slit at 10×10 cm^2 field size at source-to-imager distance (SID) of 153 cm. The slit was formed by a pair of tungsten alloy blocks that were tilted by 1.5° and placed on top of the imager with a separation of 100 μm. Following the procedure developed by Fujita *et al.*, a finely sampled line spread function (LSF) was obtained from the slit image, and Fourier transform of the LSF yielded the MTF (Fujita *et al.*, 1992). The experiment has been described in great details in Rottmann *et al.* (Rottmann *et al.*, 2016).

The qNNPS is the product of the normalized NPS (NNPS) and the average incident x-ray fluence (q) at the EPID surface. To calculate NNPS, 250 flood field images were obtained with 10×10 cm^2 field size at 180 cm SID. A central area of 120×120 pixels was obtained to compute a 2D NNPS, which was further converted into a 1D NNPS. The reference q at 100 cm SID was derived in a previous study (Star-Lack *et al.*, 2014) and the q value at 153 cm SID was adjusted by inverse square correction. The experiment has been described in great details in Rottmann *et al.* (Rottmann *et al.*, 2016).

DQE was calculated from MTF and qNNPS according to:

$$\mathbf{DQE = MTF^2/qNNPS} \tag{1}$$

2.1.4. Simulation of MTF, qNNPS, and DQE

For MTF simulation, a 0.1 mm × 70 mm planar photon source tilted by 1.5° was placed above the EPID surface. Ten million primary photons were uniformly generated towards the imager model. Optical photons entering each pixel of the panel detector were recorded to generate the image. The beam model was described in Section 2.1.2. Following the Fujita method, the MTF was computed from a finely sampled LSF

24

obtained from the slit image. The statistical uncertainty calculated from the number of detected optical photons in the slit area was less than 0.3%.

For qNNPS simulation, the same slit image as the MTF simulation was used and Fujita-Lubberts-Swank (FLS) method was employed (Star-Lack *et al.*, 2014). Point spread function (PSF) produced by each detected x-ray photon was collected and summed along one dimension to form a 1D PSF. The corresponding NPS was calculated following:

$$\mathbf{NPS_i(f) = |DFT(PSF_i)|^2} \tag{2}$$

where **i** is the photon index and DFT is discrete Fourier transform. The final NPS(f) was obtained by averaging $NPS_i(f)$ over all detected photons. Then, qNNPS(f) was calculated as:

$$\mathbf{qNNPS(f) = \frac{NPS(f)}{QE \times Swank\ factor \times NPS(f)_{max}}} \tag{3}$$

where QE is the estimated photon detection efficiency, and $NPS(f)_{max}$ is the maximum NPS value. Swank factor representing the SNR decrease was obtained from the scintillation pulse height spectrum (Swank, 1973). A detailed description of the qNNPS simulation can be found in a previous study (Star-Lack *et al.*, 2014).

2.1.5. Validation of AS1200 model

The measured and simulated metrics were compared using with the normalized root-mean-squared-error (NRMSE) following:

$$\mathbf{NRMSE = \sqrt{\frac{\sum_{i=1}^{N}(simu_i - meas_i)^2}{N}} / (meas_{max} - meas_{min})} \tag{4}$$

where N is the number of sample bins in the frequency domain, 'simu' and 'meas' refer to the simulated and measured value, respectively. A NRMSE value close to zero indicates a good agreement between measurement and simulation.

25

2.1.6. Study of optical properties on imager performance

Imager models with different phosphor thickness, phosphor grain size, phosphor RI, binder RI, and packing ratio were tested to evaluate their impact on EPID imaging performance. These tests were conducted utilizing the validated AS1200 model.

Phosphor thickness of 0.15 mm, 0.29 mm, 0.5 mm, 0.75 mm, and 1 mm were implemented. Thickness of 0.29 mm was used as the reference value. The property impact was quantified using the NRMSE:

$$\mathbf{NRMSE} = \sqrt{\frac{\sum_{i=1}^{N}(X_i(n) - X_i(ref))^2}{N}} \Big/ \left(X_{max}(ref) - X_{min}(ref)\right) \qquad (5)$$

where X is the image quality metric (either qNNPS or MTF), 'ref' and 'n' refers to the reference value and the tested value of the optical property under consideration, respectively. Each tested phosphor thickness was compared to the reference test, and the corresponding NRMSE was calculated for qNNPS and MTF. A large NRMSE is indicative of a large deviation from the reference. Other optical properties tested are phosphor grain size of 5 μm, 6 μm, 7* μm, 8 μm, 9 μm, phosphor RI of 1.1, 1.3, 1.5, 2, 2.3*, 3, binder RI of 1*, 1.35, 1.5, and packing ratio of 0.1, 0.2, 0.3, 0.4, 0.5, 0.62*. Reference values are marked by "*". Each property was conducted in the same way as the phosphor thickness. Along with the qNNPS and MTF, DQE(0) was also calculated for each property value according to:

$$\mathbf{DQE(0)} = \mathbf{1/qNNPS(0)} \qquad (6)$$

2.2. Results

2.2.1. AS1200 model validation

The measured and simulated MTF, qNNPS, and DQE curves of AS1200 imager are shown in Figure **3**. The NRMSE value is 0.0467 for MTF, 0.0217 for qNNPS, and 0.0885 for DQE, all indicating a good agreement between measurement and simulation.
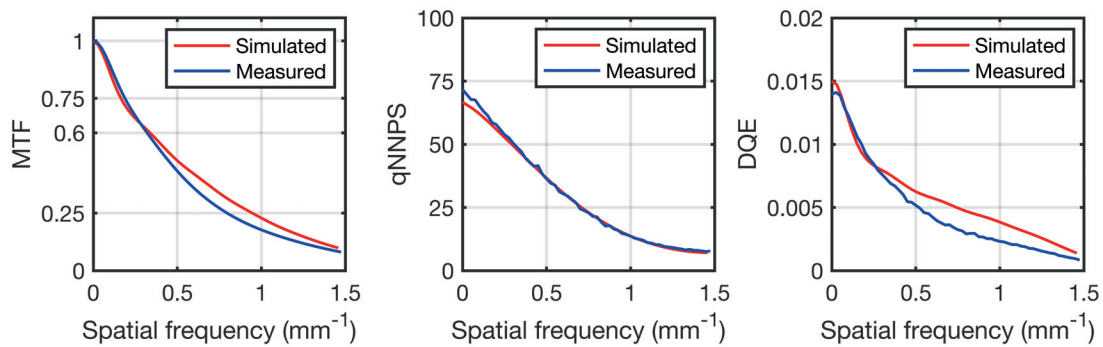
Figure 3 Comparison of MTF (left), qNNPS (middle), and DQE (right) of AS1200 imager between simulation and measurement.

2.2.2. Study of phosphor grain size

The qNNPS and MTF curves are compared at different phosphor grain sizes in Figure **4**. Both qNNPS and MTF decrease with increasing grain size. As shown in Table **3**, larger NRMSE values are observed in qNNPS than that in MTF, demonstrating a greater impact of grain size on qNNPS than on MTF.
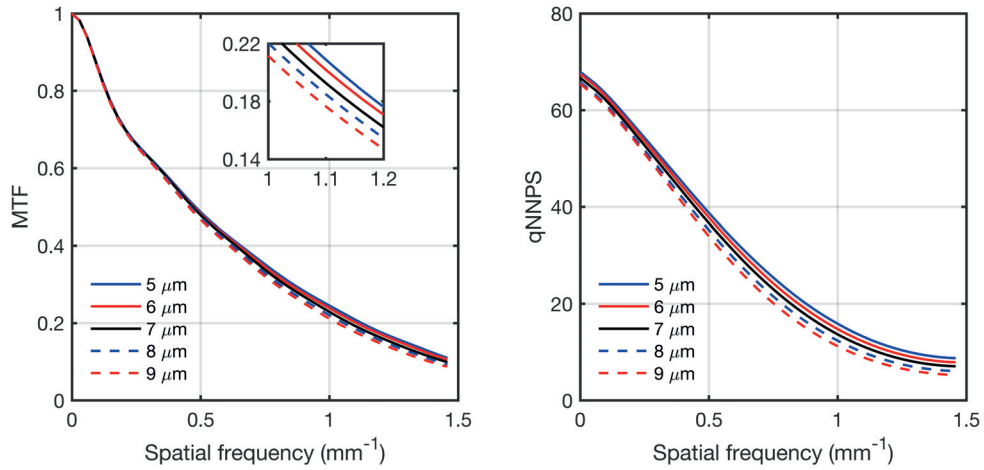
Figure 4 Simulation results of MTF and qNNPS with varying phosphor grain size. The inserted smaller figure is the same data plotted over the spatial frequency range of 1 mm^{-1} to 1.2 mm^{-1}.

Table 3 NRMSE of MTF and qNNPS with respect to the reference value and DQE(0) for each grain size.

Parameters	5 μm	6 μm	7 μm	8 μm	9 μm
MTF	1.24%	0.69%	0	0.72%	1.46%
qNNPS	3.29%	1.71%	0	2.06%	3.79%
DQE(0)	0.0147	0.0148	0.015	0.0152	0.0153

2.2.3.   Study of phosphor thickness

As shown in Figure **5**, both qNNPS and MTF curves decrease with increasing phosphor thickness. The impact of phosphor thickness is greater on qNNPS than that on MTF, as indicated by the larger NRMSE values in Table **4**.

28
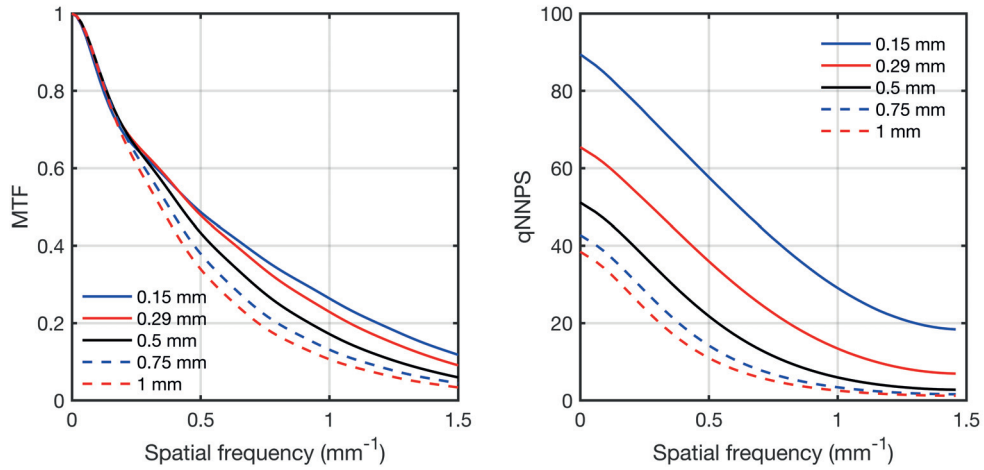
Figure 5 Simulation results of MTF and qNNPS with varying phosphor thickness.

Table 4 NRMSE of MTF and qNNPS with respect to the reference value and DQE(0) for

each phosphor thickness.

Phosphor thickness	0.15 mm	0.29 mm	0.5 mm	0.75 mm	1 mm
MTF	2.69%	0	4.86%	8.94%	11.76%
qNNPS	32.32%	0	19.05%	28.96%	33.57%
DQE(0)	0.0112	0.015	0.0196	0.0234	0.026

2.2.4.   Study of phosphor refractive index

As shown in Figure **6**, increasing the phosphor RI increases both qNNPS and MTF.

As listed in Table **5**, phosphor RI has greater impact on qNNPS than on MTF.

29
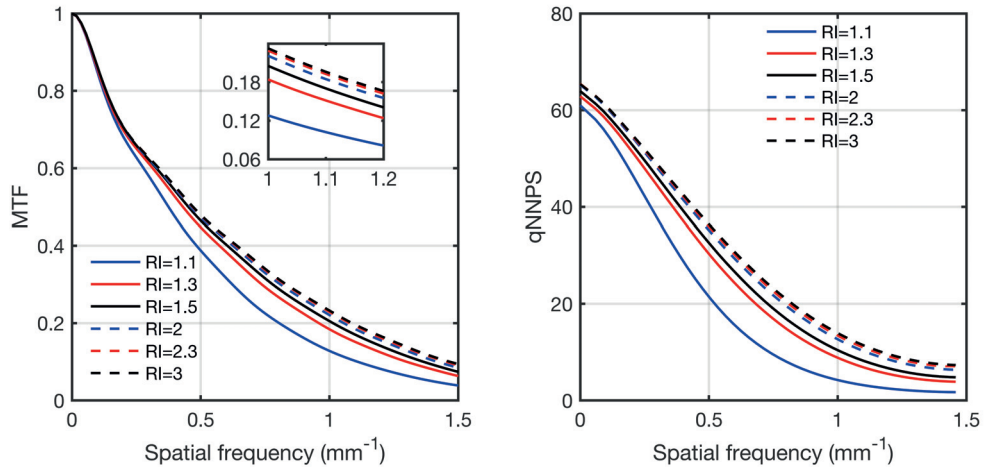
Figure 6 Simulation results of MTF and qNNPS with varying phosphor RI. The inserted smaller figure is the same data plotted over the spatial frequency range of 1 mm^{-1} to 1.2 mm^{-1}.

Table 5 NRMSE of MTF and qNNPS with respect to the reference value and DQE(0) for each phosphor RI.

Phosphor RI	1.1	1.3	1.5	2.0	2.3	3.0
MTF	8.96%	3.69%	1.92%	0.69%	0	0.27%
qNNPS	17.42%	7.64%	4.8%	1.15%	0	0.73%
DQE(0)	0.0164	0.0159	0.0156	0.0153	0.015	0.0153

2.2.5.   Study of binder refractive index

As shown in Figure **7**, increasing the binder RI degrades the qNNPS and MTF. The NRMSE values listed in Table **6** indicate that the impact of the binder RI on the qNNPS is greater than that on MTF.

30
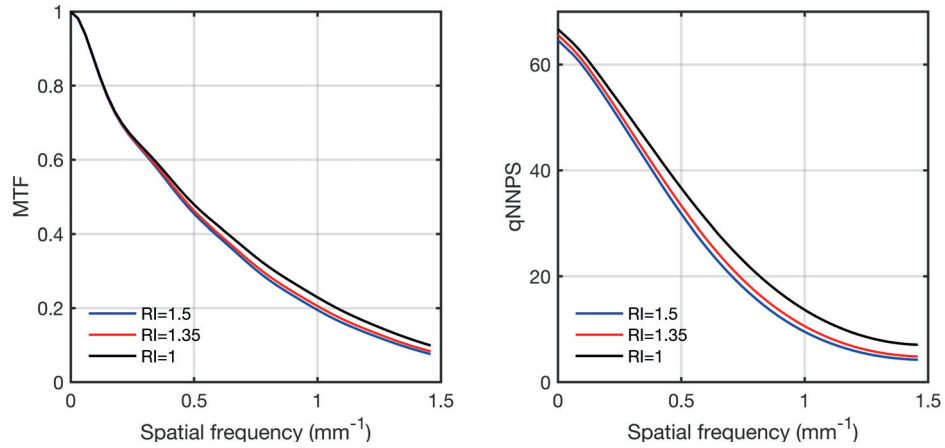
Figure 7 Simulation results of MTF and qNNPS with varying binder RI.

Table 6 NRMSE of MTF and qNNPS with respect to the reference value and DQE(0) for

each binder RI.

Binder RI	1.0	1.35	1.5
MTF	0	2.0%	2.9%
qNNPS	0	4.7%	6.6%
DQE(0)	0.015	0.0152	0.0155

2.2.6. Study of packing ratio

As shown in Figure **8** and Table **7**, increasing the packing ratio increases the qNNPS and MTF, and the impact of the packing ratio on qNNPS is much greater than that on MTF.
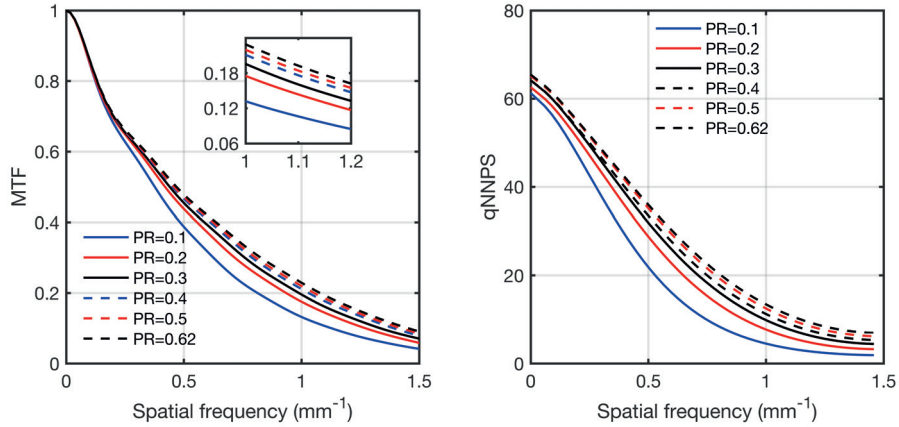
Figure 8 Simulation results of MTF and qNNPS with varying packing ratio. The inserted smaller figure is the same data plotted over the spatial frequency range of 1 mm^{-1} to 1.2 mm^{-1}.

Table 7 NRMSE of MTF and qNNPS with respect to the reference value and DQE(0) for each packing ratio.

Packing ratio	0.1	0.2	0.3	0.4	0.5	0.62
MTF	8.69%	4.55%	2.78%	1.45%	0.77%	0
qNNPS	16.86%	9.56%	5.63%	3.55%	1.31%	0
DQE(0)	0.0163	0.016	0.0156	0.0156	0.0153	0.015

2.3.   Discussion

In this chapter, an AS1200 EPID model was developed and validated against measurement. The NRMSE values between measured and simulated qNNPS, MTF, and DQE were 0.0217, 0.0467, and 0.0885, respectively. DQE had a slightly higher NRMSE value, because it is calculated from MTF and qNNPS, and deviation from both parameters was propagated to DQE. Small deviations of the simulated DQE in the low frequency regions are attributed a corresponding decrease in qNNPS. The discrepancy at

32

qNNPS(0) may be caused by the different approaches of acquiring qNNPS curves during simulation and measurement. The measured qNNPS curve was acquired following the standard procedure and the qNNPS(0) was estimated through extrapolation. The simulated qNNPS curve was acquired using the FLS method, which generates an explicit estimate for qNNPS(0). Such a computation difference may introduce a discrepancy at qNNPS(0). The deviation of the simulated DQE at middle frequencies is caused by a mismatch of MTF. Instead of simulating two tungsten blocks to form the slit, a narrow rectangular planar source was modeled and placed right above the imager for image simulation. This source model may cause a narrower line spread function and an overestimation of MTF values.

DQE(0) increases significantly with the phosphor thickness but is not substantially impacted by other properties. This is because quantum detective efficiency of x-ray photons depends mainly on the phosphor thickness (Kausch *et al.*, 1999). Other properties only influence the optical photon propagation and interaction.

The MTF curve degrades with increasing grain size, phosphor thickness, and binder RI, and with decreasing phosphor RI and packing ratio, in a similar manner as qNNPS. The dependence of MTF on grain size and packing ratio agrees well with previous works (Liaparinos *et al.*, 2006; Poludniowski and Evans, 2013b). It has been shown that, a decrease in grain fraction within the phosphor layer, equivalent to lower packing ratio and larger grain size, will cause a decrease in optical photon scattering events. This further causes a worse directivity of photon flux propagation through the imager, leading to a degraded MTF. A high binder RI and a low phosphor RI, equivalent to a low relative RI, result in smaller scatter angles and a worse directivity of photon flux propagation,

33

further leading to a degraded MTF. Similar results can be found in previous study (Poludniowski and Evans, 2013a). The negative impact of phosphor thickness on MTF is due to the increased scatter of optical photons that allows a greater later spread (Kausch *et al.*, 1999).

The qNNPS decreases with an increase in phosphor grain size, phosphor thickness, and binder RI, as well as with a decrease in phosphor RI and packing ratio. For the grain size, the optical photons tend to scatter at small angles along the incident direction as a result of large grain size, leading to less noise and degrading qNNPS. For the phosphor thickness, a thicker phosphor allows greater x-ray photon absorption and optical photon emission, providing a better noise performance. Also, optical photons scatter at smaller angles at a larger binder RI. This can be explained with the relative RI of grain to binder, which is defined as the ratio of grain RI to binder RI. The optical photons scatter at smaller angles with a lower relative RI (Poludniowski and Evans, 2013a). With fixed grain RI, a large binder RI reduces the relative RI, producing smaller scatter angles, less noise, and degrading qNNPS. This also explains the impact of phosphor RI. With fixed binder RI, a small phosphor RI reduces the relative RI, producing smaller scatter angles and degrading qNNPS. Regarding the packing ratio, a lower packing ratio leads to fewer grains in phosphor. Therefore, the optical photons scatter fewer times before exiting the phosphor, leading to less noise and degrading qNNPS.

It is challenging to offer an optimal configuration of EPID phosphor optical properties because the configuration depends on specific imaging task and user's expectation. For MTF-weighted optimization, a thin phosphor layer with small grain size, large relative RI, and large packing ratio would be a good option. Alternatively, a

qNNPS-weighted optimization requires a thick phosphor consisting of large grain size, small relative RI and small packing ratio. Since qNNPS shows greater response to optical property variation, an intensively degraded noise performance is expected during MTF-weighted optimization. Phosphor thickness is the major issue to consider for DQE-weighted optimization. An EPID imager with the thick phosphor (up to 1 mm) would be preferred (Kausch *et al.*, 1999).

2.4. Conclusion/Recommendation

In this chapter, a MC model of the AS1200 imager was developed and validated with experimental data. Both radiative and optical photon transport were simulated in the model. The impact of five phosphor optical properties on qNNPS, MTF, and DQE(0) was fully investigated to show how these parameters affect x-ray absorption, optical photon scattering, and overall EPID performance. With a complete understanding of the optical photon interactions within the imager, simulations of EPID imagers can be performed for specific clinical applications in the future.

2.5. Reference

Agostinelli S, Allison J, Amako K a, Apostolakis J, Araujo H, Arce P, Asai M, Axen D, Banerjee S and Barrand G 2003 GEANT4—a simulation toolkit *Nuclear instruments and methods in physics research section A: Accelerators, Spectrometers, Detectors and Associated Equipment* **506** 250-303

Allison J, Amako K, Apostolakis J, Araujo H, Dubois P A, Asai M, Barrand G, Capra R, Chauvie S and Chytracek R 2006 Geant4 developments and applications *IEEE Transactions on Nuclear Science* **53** 270-8

Antonuk L E 2002 Electronic portal imaging devices: a review and historical perspective of contemporary technologies and research *Phys Med Biol* **47** R31-65

Constantin M, Perl J, LoSasso T, Salop A, Whittum D, Narula A, Svatos M and Keall P J 2011 Modeling the truebeam linac using a CAD to Geant4 geometry implementation: dose and IAEA-compliant phase space calculations *Med Phys* **38** 4018-24

Fujita H, Tsai D Y, Itoh T, Doi K, Morishita J, Ueda K and Ohtsuka A 1992 A simple method for determining the modulation transfer function in digital radiography *IEEE Trans Med Imaging* **11** 34-9

Grevillot L, Frisson T, Maneval D, Zahra N, Badel J N and Sarrut D 2011 Simulation of a 6 MV Elekta Precise Linac photon beam using GATE/GEANT4 *Phys Med Biol* **56** 903-18

Jan S, Benoit D, Becheva E, Carlier T, Cassol F, Descourt P, Frisson T, Grevillot L, Guigues L, Maigne L, Morel C, Perrot Y, Rehfeld N, Sarrut D, Schaart D R, Stute S, Pietrzyk U, Visvikis D, Zahra N and Buvat I 2011 GATE V6: a major enhancement of the GATE simulation platform enabling modelling of CT and radiotherapy *Phys Med Biol* **56** 881-901

Kausch C, Schreiber B, Kreuder F, Schmidt R and Dossel O 1999 Monte Carlo simulations of the imaging performance of metal plate/phosphor screens used in radiotherapy *Med Phys* **26** 2113-24

Liaparinos P F, Kandarakis I S, Cavouras D A, Delis H B and Panayiotakis G S 2006 Modeling granular phosphor screens by Monte Carlo methods *Med Phys* **33** 4502-14

Maigne L, Perrot Y, Schaart D R, Donnarieix D and Breton V 2011 Comparison of GATE/GEANT4 with EGSnrc and MCNP for electron dose calculations at energies between 15 keV and 20 MeV *Phys Med Biol* **56** 811-27

Myronakis M, Star-Lack J, Baturin P, Rottmann J, Morf D, Wang A, Hu Y H, Shedlock D and Berbeco R I 2017 A novel multilayer MV imager computational model for component optimization *Med Phys* **44** 4213-22

Poludniowski G G and Evans P M 2013a Optical photon transport in powdered-phosphor scintillators. Part 1. Multiple-scattering and validity of the Boltzmann transport equation *Med Phys* **40** 041904

Poludniowski G G and Evans P M 2013b Optical photon transport in powdered-phosphor scintillators. Part II. Calculation of single-scattering transport parameters *Med Phys* **40** 041905

Rottmann J, Morf D, Fueglistaller R, Zentai G, Star-Lack J and Berbeco R 2016 A novel EPID design for enhanced contrast and detective quantum efficiency *Phys Med Biol* **61** 6297-306

Sarrut D, Bardiès M, Boussion N, Freud N, Jan S, Létang J M, Loudos G, Maigne L, Marcatili S and Mauxion T 2014 A review of the use and potential of the GATE Monte Carlo simulation code for radiation therapy and dosimetry applications *Medical physics* **41**

Shi M, Myronakis M, Hu Y H, Morf D, Rottmann J and Berbeco R 2018 A Monte Carlo study of the impact of phosphor optical properties on EPID imaging performance *Phys Med Biol* **63** 165013

Siewerdsen J H, Antonuk L E, el-Mohri Y, Yorkston J, Huang W and Cunningham I A 1998 Signal, noise power spectrum, and detective quantum efficiency of indirect-detection flat-panel imagers for diagnostic radiology *Med Phys* **25** 614-28

Star-Lack J, Sun M, Meyer A, Morf D, Constantin D, Fahrig R and Abel E 2014 Rapid Monte Carlo simulation of detector DQE(f) *Med Phys* **41** 031916

Swank R K 1973 Absorption and noise in x‐ray phosphors *Journal of Applied Physics* **44** 4199-203

36

III.   A NOVEL, FAST METHOD FOR EPID IMAGE SIMULATION

In this chapter, a novel technique for fast simulation of EPID planar image, FastEPID, is developed and validated against measurement and conventional MC simulation. The proposed FastEPID method utilizes pre-calculated imager response, such as photon energy deposition efficiency and optical spread function (OSF), to generate image without simulating particle transport within the imager. Validation of the FastEPID method is performed by evaluating the differences in MTF and images of a Las Vegas phantom and an anthropomorphic pelvis phantom between simulation and measurement. We demonstrate a significant decrease in the simulation time without compromising simulation accuracy.

This chapter is based on published work: Shi M, Myronakis M, Hu Y H, Jacobson M, Lehmann M, Fueglistaller R, Huber P, Baturin P, Wang A, Ferguson D, Harris T, Morf D and Berbeco R. A novel method for fast image simulation of flat panel detectors. *Phys Med Biol.* **64**, 095019 (2019) (Shi *et al.*, 2019).

3.1.   Method and materials

3.1.1. Pre-calculation of the imager response and FastEPID simulation

The FastEPID method requires pre-calculation of x-ray energy deposition efficiency (η) values and optical spread functions (OSFs), generated utilizing the validated AS1200 model described in chapter 2. During image simulation, the ηs and OSFs are imported and utilized by a "FastEPID" GATE actor to generate the image. Actor is a user-defined tool attached to a given volume for a specific purpose. Both ηs

37

and OSFs are unique to a specific imager. Therefore, simulation of a new imager utilizing the proposed FastEPID method will require a re-calculation of OSFs and ηs.

3.1.1.1. Pre-calculation of ηs and OSFs

For a given incident photon energy, a mono-energetic photon pencil beam is placed above the imager surface and emits photons right at the central pixel. The total energy deposition in the GOS phosphor is recorded. Energy deposition efficiency, η, is then calculated as the ratio of the total energy deposition to the total incident energy. The output image is acquired and OSF is calculated following:

$$\textbf{OSF} = \textbf{Output\_image}/(N_{incident} \times \textbf{η}) \qquad (7)$$

where $N_{incident}$ is the number of x-ray photons incident on the EPID model. The OSF represents the optical spread function due to a full energy deposition of an incident photon. Size of the OSFs can be optimized by balancing the reduction in simulation time with the accuracy of the simulated image quality. A separate test optimizing the OSF size is explained in Section 3.1.3 with results shown in 3.2.1.
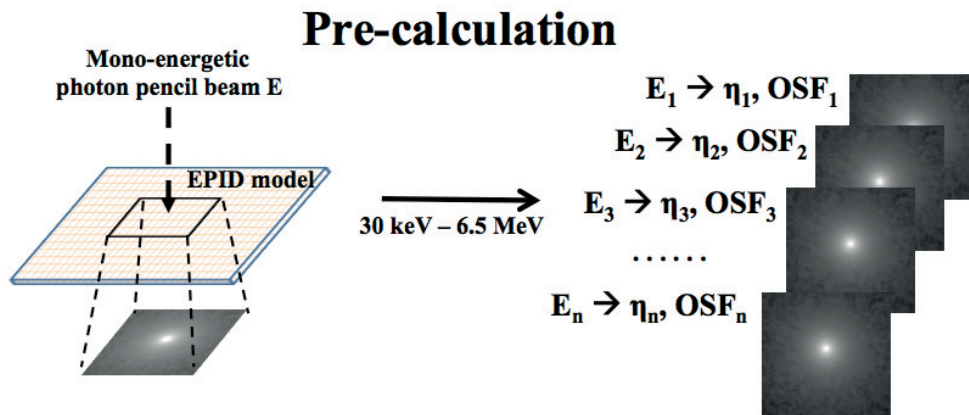
Figure 9 Workflow of the pre-calculation of OSFs and η values.

The OSFs and ηs are collected for a range of incident energies that matches a 6MV treatment beam spectrum. For each energy level, 10^7 primary photons are simulated,

giving a statistical uncertainty of less than 0.3%. The workflow of the pre-calculation process is shown in Figure **9**. Figure **10** shows the calculated η values as a function of incident photon energy.
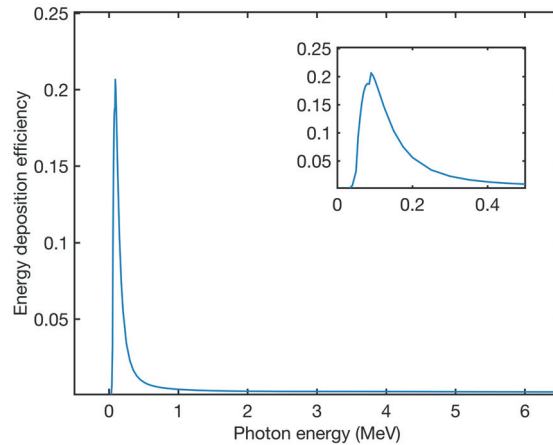
Figure 10 Energy deposition efficiency η as a function of photon energy.

3.1.1.2.   FastEPID simulation

During the FastEPID simulation, the beam source and the phantom are modeled the same as in the conventional simulation. A virtual detector, normally a dummy air slab, replaces the AS1200 imager model. The virtual detector has the same pitch (0.336 mm) as the AS1200 imager. The detector size varies with imaging tasks. In this chapter, the size of the virtual detector was set to $225 \times 225 \times 1$ mm^3, unless stated otherwise. The detector is placed with its surface aligned with the panel detector surface instead of the AS1200 top surface, avoiding any inverse square correction. The SID is set to 153.5 cm for both conventional and FastEPID simulations (Rottmann *et al.*, 2016), unless otherwise stated.

For each photon incident on the virtual detector, the corresponding pre-calculated η and OSF are calculated through linear interpolation according to the photon energy. Photon detection is determined based on the comparison between a random number (RN)

39

and η. If η ≥ RN, the incident photon is "detected", and the corresponding OSF is added to the EPID image with the center aligned to the incident position. If η < RN, the incident photon is discarded and the simulation continues to the next history. If the photon energy falls outside of the range of 0.03-6.5 MeV, it is discarded as well. The workflow is shown in Figure **11**.
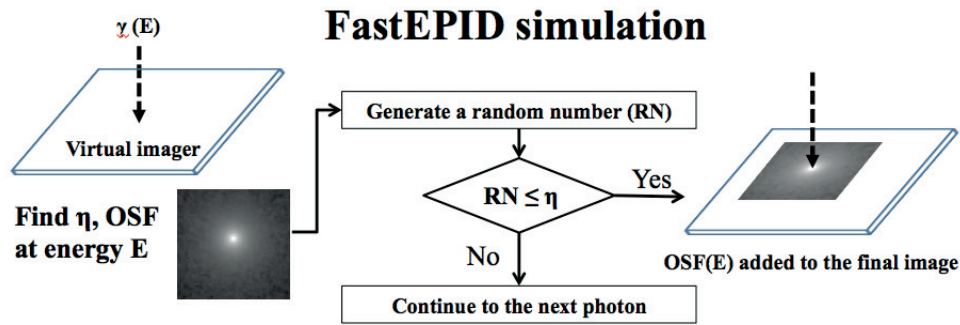
Figure 11 Workflow of FastEPID simulation.

Both primary and scattered photons are forced to fall perpendicularly on the virtual detector at the center of a single pixel. Contaminated electrons from the beam source are not considered because they would be shielded by the imager copper layer and would not contribute to the image.

3.1.2. Monte Carlo simulation environment

In this study, both the conventional and FastEPID simulations were performed with GATE v7.2 and 8.0, and Geant4 v10. Simulations were performed on either a Linux system workstation of 12 CPUs (3.8 GHz, 16 GB RAM) or on high performance computing cluster of 2000 CPU cores (CPU model and RAM vary with the assigned core, Linux operating system). The conventional simulation of AS1200 is described in greater detail in Section 2.1.2.

3.1.3. FastEPID optimization

The OSF size can vary from a small area to the size of an EPID. Since pixels outside the OSF are excluded from image generation, selecting too small OSF size may cause the image to suffer under-estimated pixel values. On the other hand, selecting too large OSF size would cause more computation time on OSF interpolation, potentially negating any reductions in the computation time.

The OSF size can be optimized by balancing the improvement in simulation time with the accuracy of the FastEPID simulated image quality. A 4×4 cm^2 open field image was simulated by the conventional MC method and used as the reference. The same images were FastEPID simulated with OSF sizes varying from 11×11 pixels to 401×401 pixels. 10^8 primary photons were delivered for each image simulation. A multi-point source (MPS) modeled from Varian TrueBeam 6 MV phase space files was utilized as the beam source in this study. The description and validation of MPS can be found in Appendix 1.

The FastEPID simulated images were compared to the conventional simulated image for each OSF size. The relative difference (Diff%) of pixel value is calculated as follows:

$$\mathbf{Diff}\%(\mathbf{x}, \mathbf{y}) = \frac{|\mathbf{I_{FastEPID}(x,y)} - \mathbf{I_{ref}(x,y)}|}{\mathbf{max\,(I_{ref})}} \times \mathbf{100}\% \tag{8}$$

where x and y refer to pixel indices, I represents the pixel value, subscript ref refers to the conventional simulated image, and max represents the maximum pixel value in the image. Images were normalized to the mean value before comparison. Passing rate (PR) was calculated to quantify the agreement between FastEPID and conventional simulation, which was the ratio of pixels having a Diff% less than 3%. The ratio of FastEPID

41

simulation time to the conventional simulation time was also calculated. The optimal OSF size was found at the lowest time ratio with at least 95% PR.

3.1.4. Validation studies

FastEPID simulation with the optimal OSF size was validated against measurements and the conventional simulation by utilizing MTF, signal-to-noise ratio (SNR), CNR, contrast, and PR at different Diff%. MTF was obtained using the Fujita method, and the other metrics were computed from Las Vegas (LV) phantom images. Moreover, images of an anthropomorphic pelvis phantom were simulated and compared among measurement and simulations.

3.1.4.1. Validation study with Las Vegas phantom

The FastEPID method was validated against the measurement and conventional simulation utilizing a Las Vegas (LV) phantom (Herman *et al.*, 2001). The LV phantom was placed at 100 cm source to surface distance (SSD), and the imager was placed at 153.5 cm SID with a field size of 15×15 cm^2. A central area 15×15 cm^2 of the EPID image was obtained for analysis. The multi-point source model was used as the beam source (Appendix 1). The LV phantom image was acquired experimentally with the gantry rotated by 90° and the phantom standing vertically on the treatment couch. The couch was not considered in simulation.

The simulated images were flood field (FF) corrected to remove the non-uniformities in the beam profile, and the experimentally acquired images were dark field (DF) and FF corrected to eliminate fixed pattern noise, pixel sensitivity variance and the beam profile impact (Seco and Verhaegen, 2013; Siebers *et al.*, 2004). A series of high dose FFs were simulated using the FastEPID method to correct both conventional and

FastEPID simulated images. As shown in Section 3.2.1, the flood field images simulated with the FastEPID method agreed well with that of the conventional method.

The measured and simulated EPID images were normalized to account for the different interpretation of pixel value. The pixel value was equal to the number of optical photons that entered the pixel for the simulated image, and equal to an electric signal proportional to the number of detected optical photons for the measured image. In general, the former was hundreds of times greater than the latter. Therefore, the EPID images can be normalized with a cross calibration (Seco and Verhaegen, 2013):

$$\mathbf{I_{simu\_nor}(x, y) = I_{simu}(x, y) \times \frac{I_{meas}^{100 \times 100}}{I_{simu}^{100 \times 100}}} \tag{9}$$

where $I(x, y)$ represents the value at pixel (x, y), and $I^{100 \times 100}$ is the mean value in a central area of 100×100 pixels of the image acquired at 1 MU. The subscripts $simu\_nor$, $simu$, and $meas$ indicate normalized simulation, raw simulation, and measurement, respectively.

Electronic noise is not commonly modeled in MC simulation, but cannot be removed from the measured image due to its random feature. In order to compensate for this difference, the electronic noise was reconstructed and added to the simulated EPID images. To model the electronic noise, a single frame DF image and a 200-frame averaged DF image were acquired experimentally with AS1200. The former contained fixed pattern noise and electronic noise, while the latter contained only the fixed pattern noise. Subtraction of these two DF images yielded the electronic noise, while followed a Gaussian distribution with zero mean and a standard deviation (STD) of 3.30. To compensate for the electronic noise, a Gaussian distributed image was randomly generated with the same mean and STD and then added to the simulated EPID images. In

43

general, electronic noise has a dependence on the imager, and the noise features obtained from one imager cannot be used for another imager. In this study, we kept all image acquisition on one Linac machine, and the electronic noise was reconstructed consistently. Adding electronic noise to the image would not affect the previous normalization due to the zero-mean value.
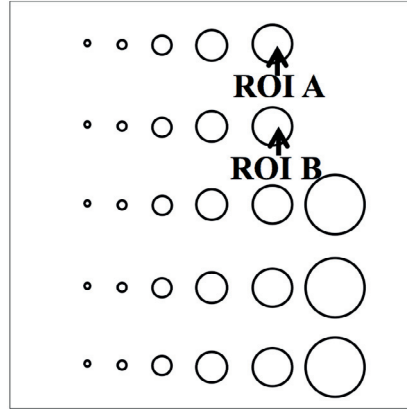
Figure 12 Regions of interest selected on Las Vegas phantom for SNR, CNR and contrast evaluation.

After correction, normalization, and noise compensation, the simulated EPID images were validated against the measured images. SNR, CNR (Bian *et al.*, 2013), and contrast of a given region-of-interest (ROI) were calculated as follows:

$$\mathbf{SNR} = \frac{S_{ROI}}{\sigma_{ROI}} \tag{10}$$

$$\mathbf{CNR} = \frac{S_{ROI} - S_{bg}}{\sqrt{(\sigma_{ROI}^2 + \sigma_{bg}^2)}} \tag{11}$$

$$\mathbf{Contrast} = \frac{S_{ROI} - S_{bg}}{S_{bg}} \tag{12}$$

where S and σ refer to the mean pixel value and standard deviation, respectively, and subscript ROI and bg denote ROI (a circular region within the phantom hole) and

44

background (a donut shaped region surrounding the ROI), respectively. SNR, CNR, and contrast were calculated for two ROIs shown in Figure **12** at 0.1 MU - 1 MU.

The relative difference of pixel value between measurement and simulations was calculated following Equation 8. For comparison between simulation and measurement, the latter was chosen as the reference image. For comparison between FastEPID and conventional simulation, the latter was chosen as the reference image. PR at Diff% < 1%, 2%, and 3% was calculated. A greater PR indicates a better agreement between the test and reference images.

3.1.4.2. Validation study with anthropomorphic pelvis phantom

Images of an anthropomorphic pelvis phantom (The Phantom Laboratory, Greenwich, NY) were experimentally acquired and FastEPID simulated in left-right (LR) direction and anterior-posterior (AP) direction at 1 MU with field size 20×20 cm^2. The measured image was DF and FF corrected. The simulated image was FF corrected, normalized, and electronic noise compensated. Gamma analysis with criteria 3%/3mm (Low *et al.*, 1998) was calculated for a quantitative evaluation of the agreement between measurement and FastEPID simulation. Pelvis phantom images were not acquired with conventional MC simulation due to impractical run time.

3.1.4.3. Validation study with MTF

The measured MTF of the AS1200 imager was acquired by using the slit image method (Fujita *et al.*, 1992) and has been described in greater detail previously (Rottmann *et al.*, 2016). A brief explanation can be found in Section 2.1.3. For the conventional simulation of MTF, a 70×0.1 mm^2 plane photon source was tilted by 1.5° and placed above the imager surface. Ten millions x-ray photons sampled from a 6 MV

45

spectrum were launched onto the imager and the optical photons incident on each pixel were collected to form the slit image. A finely sampled LSF was obtained from the slit image following the Fujita method and then converted into MTF. The FastEPID simulation was conducted in the same way with the imager model replaced by a virtual detector. Agreement between the measured, the conventionally simulated and the FastEPID simulated MTF was evaluated by MTF difference at low, middle, and high spatial frequency.

3.1.5. Improvement of the simulation time

Time ratio of the conventional simulation to the FastEPID simulation was calculated to quantify the improvement of the simulation time utilizing the FastEPID method. The ratios were calculated for the tests of the 4×4 cm^2 open field images (Section 3.1.3), 1 MU LV phantom images (Section 3.1.4), and 1 MU pelvis phantom images (Section 3.1.4).

3.2. Results

3.2.1. FastEPID optimization

Open field images obtained with the conventional and FastEPID simulations are illustrated in Figure **13**. Randomness of the subtraction between these two images (Figure **13**, right) indicates a minor pixel value variation between the FastEPID and the conventional methods. The PR at Diff% < 3% and the simulation time ratio are shown in Figure **14**. For OSF size larger than 81×81 pixels, the FastEPID simulation time is less than 1% of the conventional method and the PR is greater than 95%, indicating a substantial improvement in the simulation time without compromising the image quality.

46

Since a larger size causes longer simulation time and a smaller size results in a low PR, 81 × 81 pixels was chosen as the optimal OSF size for the following validation studies.
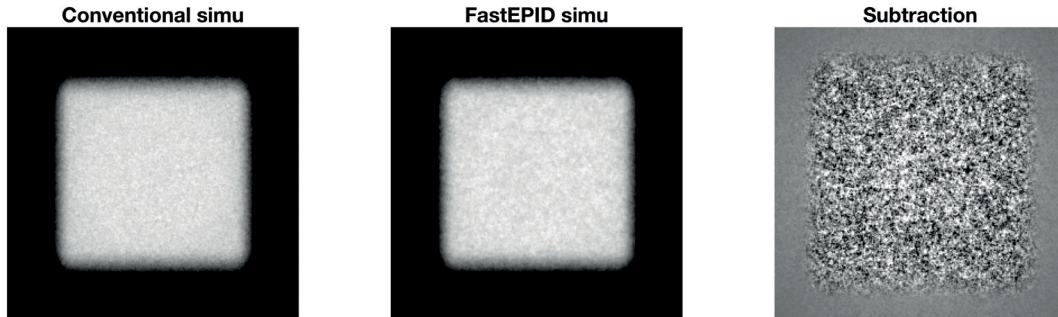
Figure 13 Open field images simulated with OSF size of 81 × 81 pixels. The image on the right shows the subtraction between conventional and FastEPID simulated images.
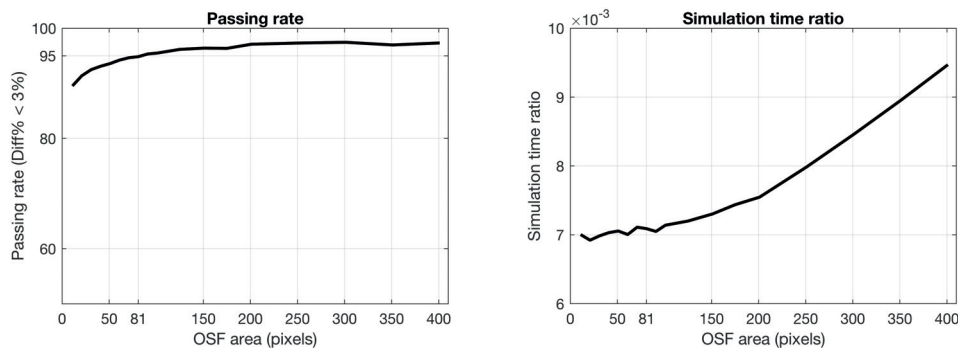
Figure 14 The passing rate and simulation time ratio of FastEPID to conventional simulation as a function of OSF area.

3.2.2. Validation study with Las Vegas phantom

LV phantom images obtained from measurement and simulations are shown in Figure **15**. The SNR, CNR, and contrast of ROI A and B are shown in Figure **16**. While the SNR and CNR are consistent between simulations and measurement in both ROIs, an overestimation of contrast was found with both simulation methods. All methods (simulation and measurement) found a similar contrast difference between ROI A and B, suggesting a systematic shift.

47
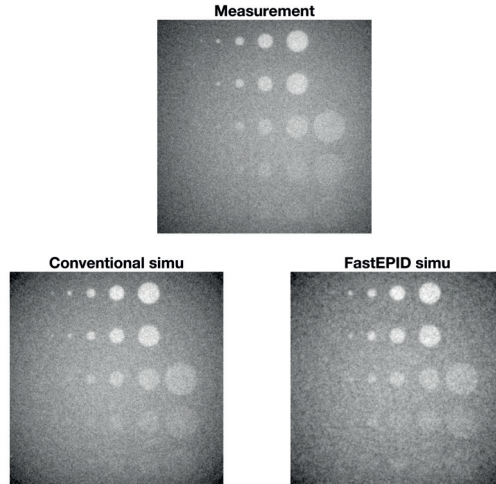
Figure 15 Las Vegas phantom images acquired by measurement, conventional

simulation, and FastEPID simulation.
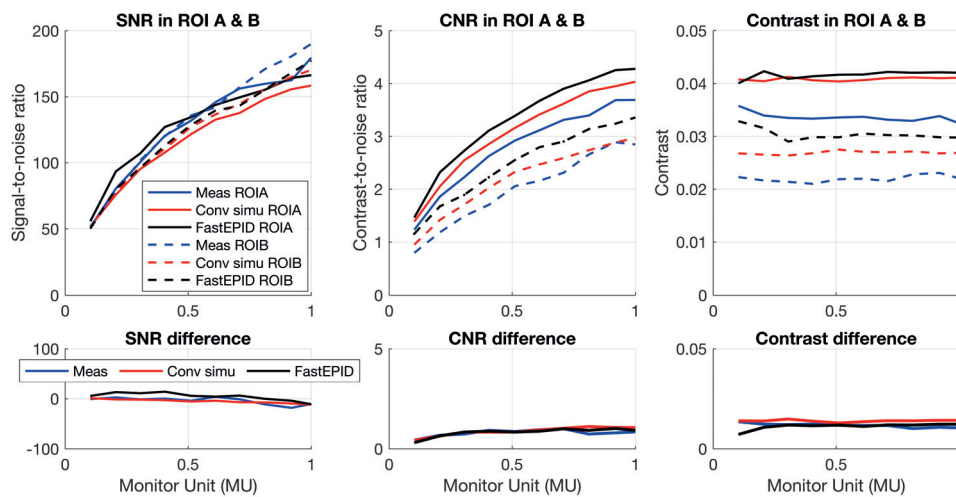
Figure 16 SNR, CNR, and contrast at ROIs A and B. Differences between the two ROIs

for each figure of merit are plotted on the bottom subplot.

The PR at Diff% < 1%, 2% and 3% between measurement and simulations are shown in Figure **17**. The FastEPID simulation provides similar agreement with measurement as the conventional simulation. The PR between the two simulations is relatively high due to less noise in the simulations. A lower PR is observed at lower MU images in all cases due to an increasing impact of stochastic noise on image quality at lower doses.

48
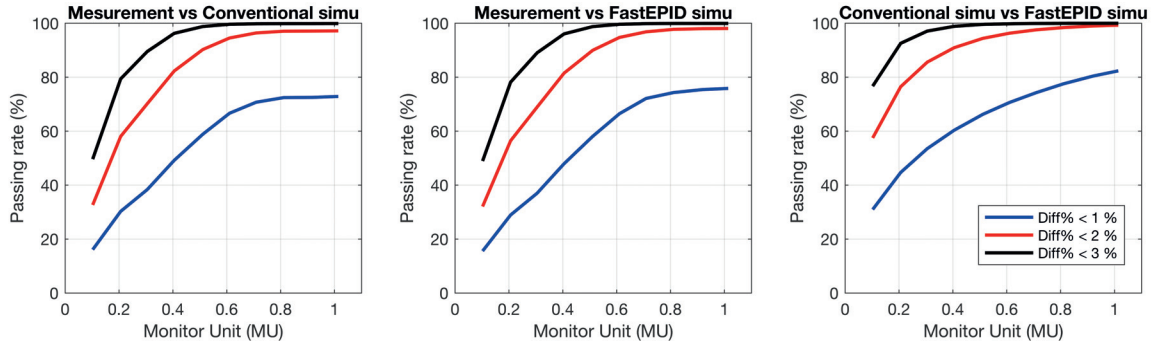
Figure 17 The passing rate at Diff% < 1%, 2%, and 3%.

3.2.3. Validation study with anthropomorphic pelvis phantom
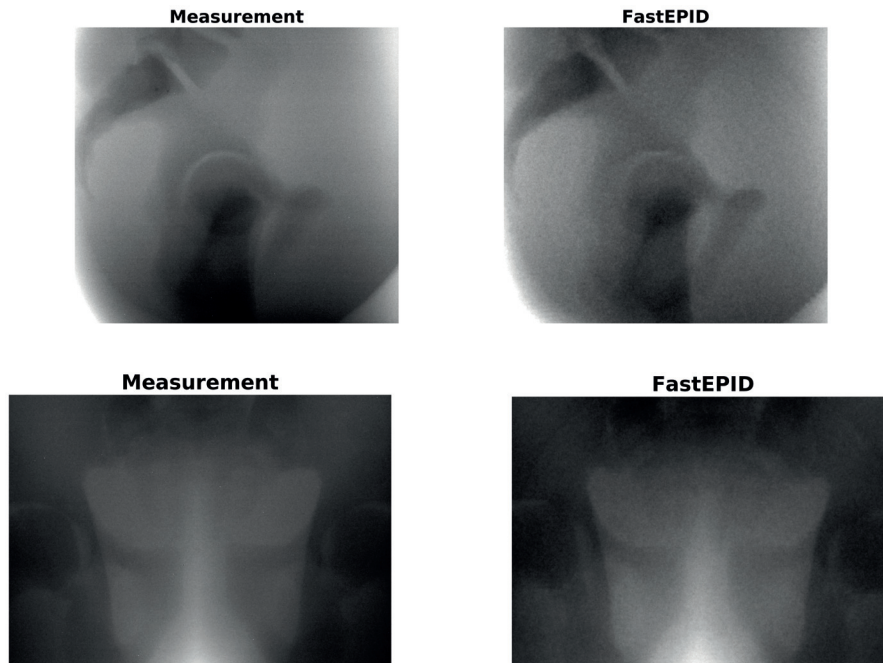
Figure 18 Pelvis phantom images (measurement versus FastEPID simulation) in left-right direction (top row) and in anterior-posterior direction (bottom row).

As shown in Figure **18**, the measured and FastEPID simulated pelvis phantom images have similar image quality, in both LR and AP directions. Gamma analysis with criteria 3%/3mm shows 85% and 90% agreement between measurement and FastEPID simulation in both projections, respectively.

49

3.2.4. Validation study with MTF

The measured and simulated MTF curves are shown in Figure **19**. The MTF difference between measurement and simulations at various spatial frequencies are list in Table **8**. The overall agreement between measurement and FastEPID simulation is similar to the agreement between measurement and conventional simulation. MTF difference between the two simulations is negligible.

Table 8 MTF differences at different spatial frequencies.

Spatial frequency (mm^{-1})	0.1	0.75	1.5
Diff (Conventional simulation, FastEPID simulation)	0.01	0.02	0.02
Diff(Measurement, Conventional simulation)	0.03	0.07	0.01
Diff (Measurement, FastEPID simulation)	0.03	0.04	0.03
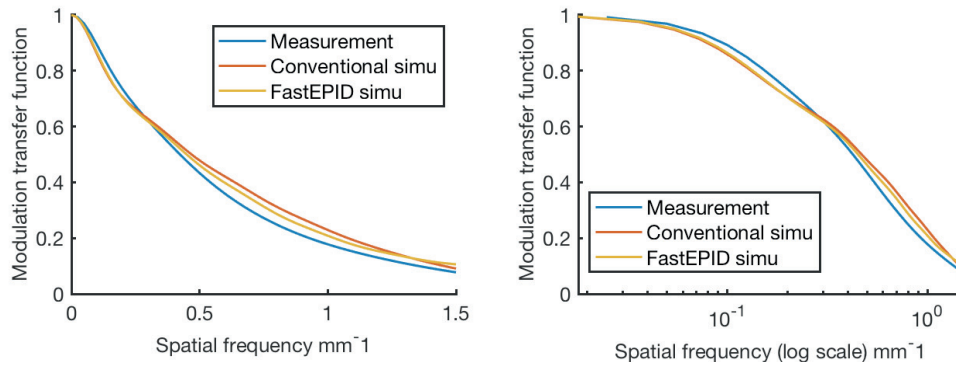
Figure 19 Modulation transfer function (MTF) acquired by measurement, conventional, and FastEPID simulations.

3.2.5. Improvement in simulation time

Run time of the EPID image simulation utilizing the conventional and FastEPID methods and the time improvement are listed in Table **9**. The FastEPID method has shortened an EPID simulation by a factor of 90-140, depending on the phantom. Since

50

particle transports in the phantom are not accelerated in this study, the time improvement is lower in thicker phantoms.

Table 9 Run time of EPID simulations.

	Open field	Las Vegas phantom	Pelvis phantom
Conventional simulation (CPU hours)	1412	1.383×10^6	No test
FastEPID simulation (CPU hours)	10	1.540×10^4	5.095×10^4
FastEPID simulation on CPU cluster	No test	8 hours	30 hours

3.3.   Discussion

We have presented a novel technique for rapid simulation of EPID image and demonstrated a significant reduction in simulation time without compromising image quality. The technique, FastEPID, utilizes pre-calculated imager responses to generate the final image without simulating particle transport in the imager model. This method strongly depends on the imager design, but not on either the beam source or the phantom. It can be implemented in multiple applications such as MV-CBCT and imager optimization.

In this study, approximately 25 CPU hours were used to develop and validate the AS1200 model, and 1000 CPU hours to pre-calculate OSFs and η values at 41 energy bins. Utilizing a 2000-core CPU cluster, these procedures took only less than an hour.

51

FastEPID simulation with optimal OSF size was validated against measurement and conventional simulation utilizing LV phantom, pelvis phantom, and MTF. For LV phantom images, FastEPID provided SNR, CNR, and contrast similar to the conventional simulation. FastEPID simulations of the pelvis phantom accurately reproduced the experimentally acquired image. Accurate predictions of MTF at low, middle, and high spatial frequencies were realized using the FastEPID method, indicating a satisfactory simulation of imager resolution. Up to 140× savings in simulation time was realized with the FastEPID method. The overall simulation time, however, depends on the phantom thickness and this factor becomes more important for human sizes. A good solution to shorten the phantom simulation time is to run the simulation on GPU, a detailed description of which can be found in chapter 5.

Electronic noise was reconstructed and added to the simulated image for a better replication of the measurement. The electronic noise has strong dependence on the imager and plays an important role, particularly on SNR and CNR, for low dose acquisitions. One application of the FastEPID method is for MV-CBCT simulation, which requires generating hundreds of low dose projections. Therefore, it is necessary to have electronic noise considered in the model.

3.4. Conclusion/Recommendation

In this chapter, a novel technique for fast EPID image simulation, FastEPID, was developed and validated. Up to 140× gain in simulation time was realized with the proposed FastEPID method without compromising image quality in terms of SNR, CNR,

52

contrast, and anatomy visualization. It is anticipated that the FastEPID method will

accelerate the development of novel MV imagers and MV-CBCT.

3.5.Reference

Bian Z, Ma J, Huang J, Zhang H, Niu S, Feng Q, Liang Z and Chen W 2013 SR-NLM: a sinogram restoration induced non-local means image filtering for low-dose computed tomography *Comput Med Imaging Graph* **37** 293-303

Fujita H, Tsai D Y, Itoh T, Doi K, Morishita J, Ueda K and Ohtsuka A 1992 A simple method for determining the modulation transfer function in digital radiography *IEEE Trans Med Imaging* **11** 34-9

Herman M G, Balter J M, Jaffray D A, McGee K P, Munro P, Shalev S, Van Herk M and Wong J W 2001 Clinical use of electronic portal imaging: report of AAPM Radiation Therapy Committee Task Group 58 *Medical Physics* **28** 712-37

Low D A, Harms W B, Mutic S and Purdy J A 1998 A technique for the quantitative evaluation of dose distributions *Med Phys* **25** 656-61

Rottmann J, Morf D, Fueglistaller R, Zentai G, Star-Lack J and Berbeco R 2016 A novel EPID design for enhanced contrast and detective quantum efficiency *Phys Med Biol* **61** 6297-306

Seco J and Verhaegen F 2013 *Monte Carlo techniques in radiation therapy*: CRC press)

Shi M, Myronakis M, Hu Y H, Jacobson M, Lehmann M, Fueglistaller R, Huber P, Baturin P, Wang A, Ferguson D, Harris T, Morf D and Berbeco R 2019 A novel method for fast image simulation of flat panel detectors *Phys Med Biol* **64** 095019

Siebers J V, Kim J O, Ko L, Keall P J and Mohan R 2004 Monte Carlo computation of dosimetric amorphous silicon electronic portal images *Med Phys* **31** 2135-46

IV. <u>FASTEPID-BASED MONTE CARLO SIMULATION OF MV-CBCT</u>

In this chapter, a MV-CBCT simulation strategy based on the FastEPID method is proposed. The reconstructed images are validated against measured data with two phantoms at multiple beam energies. We demonstrate that, by utilizing the FastEPID method, MV-CBCT simulation time can be significantly reduced without compromising the reconstruction quality for a given detector. All simulations in this chapter were conducted on a high performance computing CPU cluster.

This chapter is based on published work: Shi M, Myronakis M, Jacobson M, Lehmann M, Ferguson D, Baturin P, Huber P, Fueglistaller R, Harris T, Valencia Lozano I, Williams C, Morf D and Berbeco R. 2020 A Rapid, Accurate Image Simulation Strategy for Mega-voltage Cone-Beam Computed Tomography, *Phys Med Biol* (Shi *et al.*, 2020).

4.1. Method and materials

The proposed MV-CBCT simulation strategy was validated against measurement using a Catphan 604 phantom and an anthropomorphic pelvis phantom (The Phantom Laboratory, Greenwich, NY, USA). Measured projections of the phantoms were acquired with the AS1200 imager, while simulated projections were acquired by utilizing the FastEPID method described in chapter 3. Full scans of each phantom were acquired at beam energies 2.5 MV, 6 MV, and 6 MV FFF of Varian TrueBeam Linac. Comparison of

54

the reconstructed phantom images between measurement and FastEPID simulation was performed, and simulation time was evaluated.

4.1.1. FastEPID technique and MV-CBCT acquisition

The FastEPID simulations were executed by using GATE v7.2 and Geant4 v10.02 on a CPU cluster of 3000 cores available for each user. More details about AS1200 imager, imager model, FastEPID simulation, and CPU cluster can be found in Section 2.1.1, 2.1.2, 3.1.1, and Appendix.3, respectively.

4.1.1.1. Phantom models

The Catphan 604 phantom, often used for CBCT commissioning and quality assurance, consists of 4 scan sections. Scan section 2 contains cylindrical target inserts made from different materials and arranged in a circular pattern, as shown in Figure **20**. The phantom body is made from soft tissue equivalent urethane. An MC model of the phantom section 2 was built following the insert properties listed in Table **10** and the geometric information listed in the product manual. Two identical urethane slabs (thickness of 5.5 cm) were modeled to both ends of the phantom.

From a diagnostic CT scan, a digital version of the pelvis phantom was derived by segmenting the CT numbers into different materials with a user-defined density conversion table. The digital phantom has $512 \times 512 \times 210$ voxels with a spacing of $1 \times 1 \times 2.5$ mm^3. Properties of the phantom materials listed in Table **11** were provided by the manufacturer.
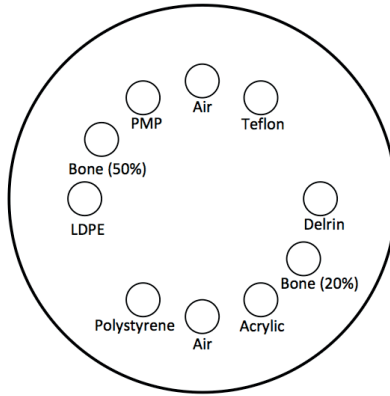
Figure 20 Schematic illustration of Catphan 604 phantom.

Table 10 Physical properties of Catphan 604 phantom.

Material	Electron density	Density (g/cm^3)	Mass composition (%)				
			N	O	C	H	Others
Air	0.001	0.00129	75.5	23.2	0.01		Ar: 1.3
Urethane	1.080	1.1	5.8	25.1	60.3	8.8	
Teflon	1.868	2.16			25		F: 75
50% Bone	1.312	1.4	6	34	35	5	P: 6, Ca: 14
20% Bone	1.084	1.14	5	30	51	5	P: 3, Ca: 6
Polystyrene	0.998	1.03			92.3	7.7	
Acrylic	1.147	1.18		32	60	8	
LDPE**	0.945	0.92			85.7	14.3	
PMP*	0.853	0.83			85.7	14.3	
Delrin	1.363	1.42		30	60	10	

*PMP: polymethylpentene, **LDPE: low density polyethylene

Table 11 Physical properties of pelvic phantom.

Material	Density (g/cm^3)	Mass composition (%)				
		N	O	C	H	Others
Bone	1.4	2.8	33.3	30.9	3.5	P: 8.8, Ca: 18.9, Sb: 1.9
Soft tissue	1.01	8.7	14.7	71.1	5.3	Sb: 0.2

4.1.1.2.   Beam source models

Phase space sources are widely accepted as the beam source in MC simulation due to the accurate characterization of particle energy spectrum, angular distribution and spatial distribution (Townson *et al.*, 2013). 2.5 MV source files were generated utilizing Varian's VirtuaLinac, a web application for MC modeling of TrueBeam, running on Amazon Web Service (Amazon Web Service, Inc., Seattle, WA, USA) (Parsons *et al.*, 2014). 6 MV and 6 MV FFF source files were provided by the manufacturer (myvarian.com/s/montecarlo, login required).

The phase space sources were validated against measurement, and the detailed information can be found in Appendix.2. The azimuthal particle redistribution (APR) technique was applied to repeatedly use the phase space sources (Bush *et al.*, 2007).

4.1.1.3.   Acquisition of phantom projections

The phantoms were placed with the center aligned to the Linac isocenter and oriented with the longitudinal axis perpendicular to the beam central axis. To match the measurement, a 30 × 30 cm^2 field size was modeled by terminating primary particles that fall beyond this area. The FastEPID virtual detector was placed at a SID of 153.5 cm (Rottmann *et al.*, 2016). During the FastEPID simulation, the phantoms rotated about

their longitudinal axis over a full arc, while the beam source and the detector were spatially fixed. Particle transports within the phantoms were simulated with the conventional MC method, and the projection images were simulated using the FastEPID method. 720 projections were acquired for each CBCT scan with an angle increment of 0.5°. The MU per projection was 0.01, 0.0167, and 0.05 at 2.5 MV, 6 MV, and 6 MV FFF, giving a total dose of 7.2 MU, 12 MU, and 36 MU, respectively. The different MU value for each energy was due to the technical constraints of the physical MV-CBCT measurements. The equivalence between the total number of primary particles and the MUs was estimated and explained in Appendix.2. The projection images were binned by four pixels along the longitudinal direction.

4.1.1.4.   MV-CBCT reconstruction algorithm

MV-CBCT images were reconstructed by using the FDK algorithm (Feldkamp *et al.*, 1984) without scatter or beam hardening correction. A Hamming filter and a cutoff at 70% of the Nyquist frequency were performed. The reconstructed volume was $290 \times 290 \times 81$ mm^3 with $1 \times 1 \times 1$ mm^3 voxel size.

The reconstructed voxel value represented the linear attenuation coefficient μ. The μ values were converted to Hounsfield units (HU) following:

$$\mathbf{HU} = \frac{\mu - \mu_{\mathbf{water}}}{\mu_{\mathbf{water}}} \times \mathbf{1000}\ \mathbf{HU} \tag{13}$$

where $\mu_{\mathbf{water}}$ denotes the mean μ of a water equivalent region. For the Catphan 604 phantom, the water equivalent region was an annular area on the uniform urethane slab that overlaps the circular pattern of the target inserts in scan section 2 (Figure **21**, right). For the pelvis phantom, the water equivalent region was a circular uniform soft tissue area (Figure **21**, left). The $\mu_{\mathbf{water}}$ value was averaged over five consecutive slices.

58
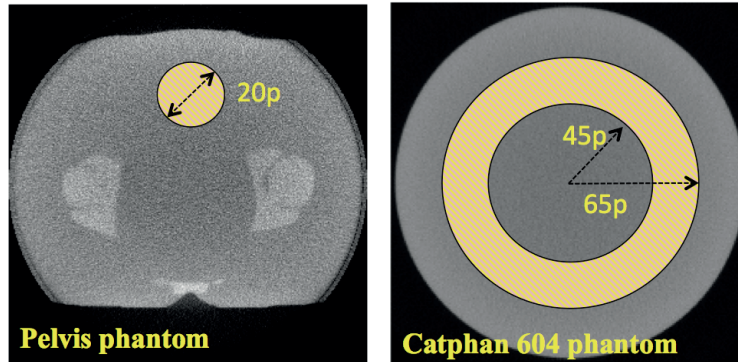
Figure 21 The selected water equivalent region in the pelvis phantom (left) and the

Catphan phantom (right).

4.1.2. Validation studies

MV-CBCT measurements were acquired on a TrueBeam Linac (v2.7 mr3) with the specifications described in Section 4.1.1.3 at Varian's Imaging Laboratory (Baden, CH). The reconstruction process was performed as described in Section 4.1.1.4. Phantom images reconstructed from the simulated projections were compared with the measurement results using multiple image metrics.

4.1.2.1. Catphan 604 study

As a measure of how faithfully the simulation captured scatter and beam hardening effects, cupping non-uniformity artifacts were evaluated in the Catphan 604 study. The artifact was quantified using the uniform urethane slab of the phantom following below:

$$\textbf{Cupping artifact} = \frac{\textbf{HU}_{\textbf{cen}} + \textbf{1000}}{\textbf{HU}_{\textbf{edge}} + \textbf{1000}} \tag{14}$$

where HU denotes the mean HU value, **cen** denotes a toroidal volume of interest (VOI) at the center of the phantom and **edge** denotes a toroidal region at the edge. Both VOIs spanned 11 axial slices. Standard deviation within these two VOIs was calculated.

59

Mean HU and contrast-to-noise ratio (CNR) were calculated and compared for the phantom target inserts. The CNR of each insert was calculated as follows:

$$CNR = \frac{HU_{ROI} - HU_{bg}}{\sqrt{(\sigma_{ROI}^2 + \sigma_{bg}^2)}} \qquad (15)$$

where HU and σ denote the mean and standard deviation of HU, respectively. Subscript ROI and bg denote a circular region within the insert and an annular region surrounding the insert, respectively. A linear relationship between the mean HU and the nominal relative electron density to water (RED) of the inserts was built for each reconstruction.

4.1.2.2. Pelvis phantom study

The pelvis phantom images were reconstructed and compared between measurement and simulation. Two regions of interest (ROI), soft tissue equivalent region and bony region (illustrated on Figure **22**), on the central image of the reconstruction volume that aligned with the beam axis were compared in terms of mean HU and standard deviation. The different bone structures appeared on the central reconstruction images was due to a 15 mm phantom position shift between simulation and measurement. The ROI RED was determined with the mean HU and the linear relationship between HU and RED derived from the Catphan 604 phantom.
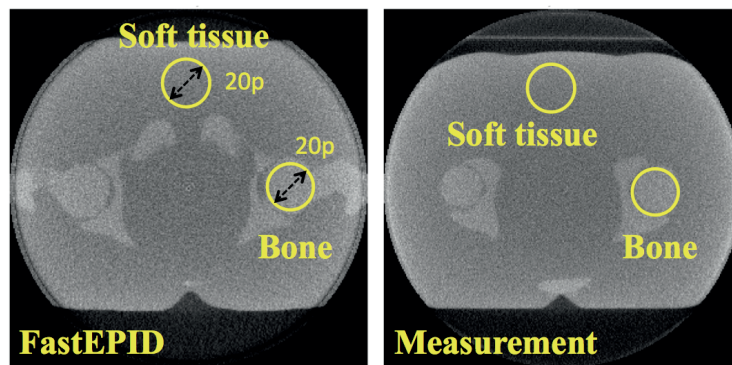
Figure 22 The regions of interest chosen for pelvis phantom analysis.

60

4.1.3. Run time of MV-CBCT simulation with the FastEPID technique

Multiple CPU models with various computation speeds were available on the CPU cluster used in this study. Simulation jobs submitted to the cluster were randomly assigned to CPU models, giving a distribution of job run time. To offer a fair estimation, the run time of each MV-CBCT simulation was scaled to the dominant CPU model, AMD Opteron™ Processor 6380 2.50 GHz, and normalized to a total dose of 1 MU. The impact of the CPU model on job run time was studied and presented in Appendix.3.

4.2. Results

4.2.1. Catphan 604 validation study

The reconstruction images of the Catphan 604 urethane slabs are displayed and compared in Figure **23**. The overall image performance agrees well between measurement and simulation at all beam energies. The quantified cupping artifact values listed in Table **12** show that the artifact captured by the FastEPID simulation was similar to that of the measurement. The standard deviations of the VOIs listed in Table **13** show a similar noise performance between measurement and simulation.

Table 12 The cupping artifact obtained with measurement and simulation.

Beam energy	Measurement	Simulation	Percent difference
2.5 MV	0.842	0.848	0.7%
6 MV	0.739	0.754	2.0%
6 MV FFF	0.816	0.824	1.0%

61
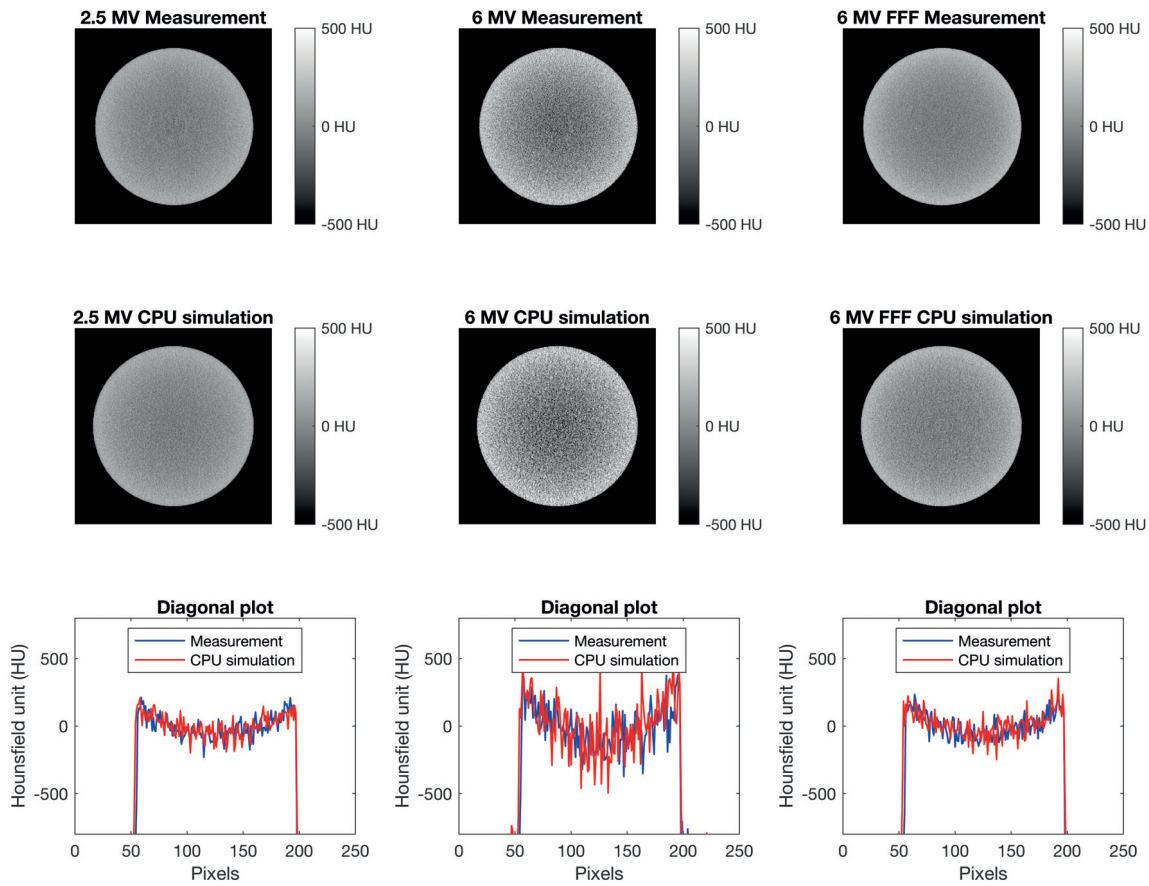
Figure 23 Reconstructed images of the Catphan 604 phantom (urethane slab slice) and

the diagonal profiles.

Table 13 The standard deviation within VOIs obtained by measurement and simulation.

VOI	Center		
Beam energy	2.5 MV	6 MV	6 MV FFF
Measurement	59.1	117.3	53.9
Simulation	56.5	149.1	64.6
VOI	Edge		
Beam energy	2.5 MV	6 MV	6 MV FFF
Measurement	45.0	102.2	48.5
Simulation	45.1	124.6	54.6
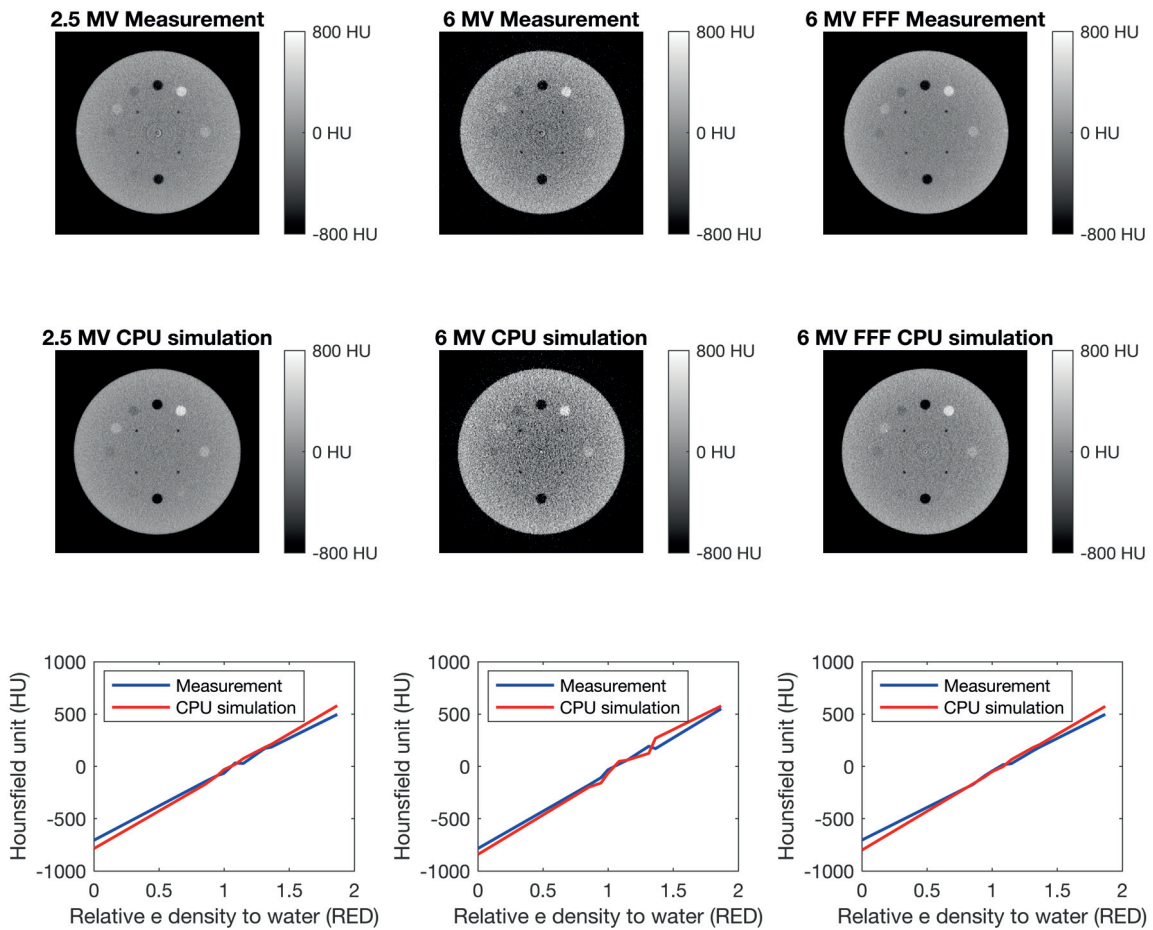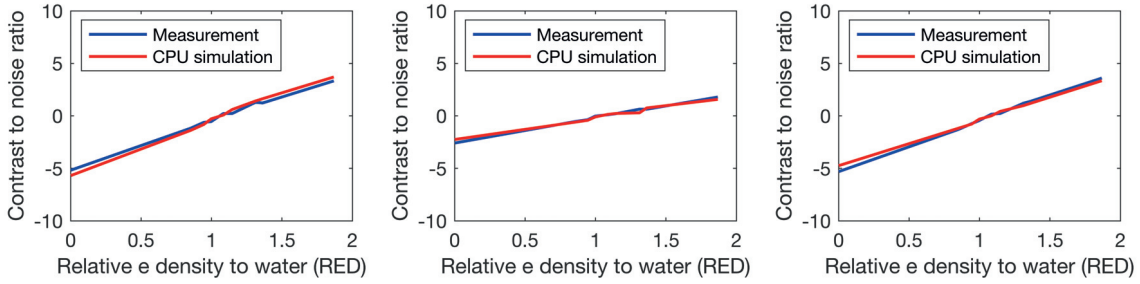
Figure 24 Reconstructed images of the Catphan 604 and the mean HU and CNR plotted against ROI relative electron density at different beam energies.

The reconstruction images of the Catphan 604 scan section 2 and the accuracy of HU and CNR at phantom inserts are displayed in Figure **24**. The simulation is able to provide similar image qualities as the measurement in terms of the overall performance, insert HU, and insert CNR. The insert HU increases linearly with the corresponding RED, indicating the possible application of MV-CBCT in dose reconstruction and treatment planning. The equations displayed in the HU plots describe the linear relationship between HU and RED.
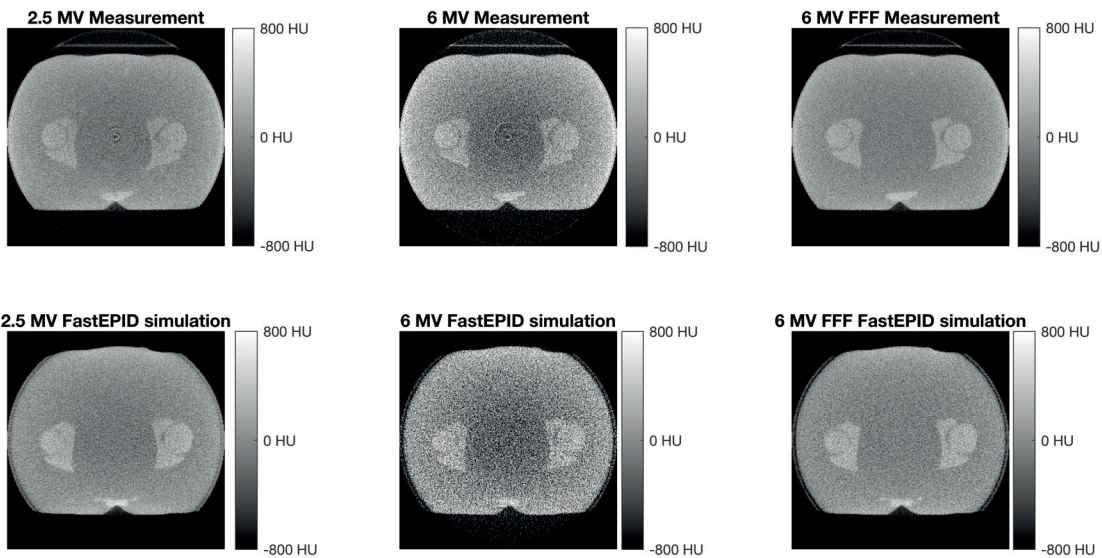
Figure 25 Reconstructed images of the pelvis phantom.

4.2.2. Pelvis phantom study

The reconstruction image of the pelvis phantom containing the same bone structure was displayed in Figure **25**, and similar image characteristics were observed between measurement and simulation at different beam energies. As listed in Table **14**, the mean HU and standard deviation of the ROIs on the central axial image indicate good agreement between measurement and simulation in terms of image signal and noise performance. The estimated RED values of the soft tissue and the bone (listed in Table **14**) are similar to the nominal values listed in Table **10**.

Table 14 The mean HU, noise, and estimated RED of the pelvis phantom at different beam energies.

	Soft tissue		
	Beam energy	Mean HU	Standard deviation	Estimated RED
	2.5	5.1	111.6	1.08
Measurement	6	-3.0	219.7	1.08
	6 FFF	-3.9	99.1	1.08
	2.5	-3.0	112.4	1.06
Simulation	6	-10.9	263.7	1.07
	6 FFF	-3.6	113.4	1.07
	Bone		
	Beam energy	Mean HU	Standard deviation	Estimated RED
	2.5	119.0	137.7	1.27
Measurement	6	188.5	239.3	1.36
	6 FFF	172.6	117.5	1.36
	2.5	152.5	130.4	1.29
Simulation	6	211.5	303.6	1.40
	6 FFF	174.5	136.6	1.35

4.2.3. Run time of MV-CBCT simulation

Run time of the MV-CBCT simulation normalized to 1 MU utilizing the FastEPID method is listed in Table **15**. The proposed FastEPID-based strategy performed on a CPU cluster was able to complete a MV-CBCT simulation within a matter of hours.

Table 15 Run time in hours of MV-CBCT simulations (normalized to 1 MU).

Beam energy	2.5 MV	6 MV	6 MV FFF
Catphan 604 phantom	31.6	35.8	19.0
Pelvis phantom	52.0	42.8	31.9

4.3. Discussion

A novel, FastEPID-based strategy for rapid MV-CBCT simulation was developed and validated in this chapter. Projections of two phantoms at different beam energies were experimentally acquired and FastEPID simulated. Phantom images reconstructed from the projections demonstrated close agreement between measurement and simulation. The run time was approximately 19 - 52 hours for FastEPID simulations executing on a CPU cluster at a total MV-CBCT dose of 1 MU. By contrast, a conventional MC simulation would require 90 - 140 times longer time, giving computations in matter of weeks or months. Thanks to the large reduction in simulation time, the proposed MV-CBCT simulation strategy can accelerate the development of new imager designs and clinical applications (Ferguson *et al.*, 2019; Hu *et al.*, 2018; Hu *et al.*, 2019; Lozano *et al.*, 2019; Rottmann *et al.*, 2016).

Cupping artifacts are generally caused by beam hardening, varying off-axis x-ray spectrum and energy-dependent EPID response, which lead to an underestimation of

66

linear coefficient in the reconstruction (Cheung *et al.*, 2009; Glover, 1982; Graham *et al.*, 2007). The cupping artifact was accurately captured by the FastEPID simulated projections. Reconstructions with 2.5 MV and 6 MV FFF beam energies demonstrated a reduced cupping artifact compared with 6 MV, which was attributed mainly to the slowly varying off-axis energy spectrum associated with the flattening filter free design (Parsons *et al.*, 2014).

No scatter or beam hardening correction was performed during the reconstruction process. The focus of this study was to evaluate the ability of FastEPID technique to rapidly and accurately simulate projections and the qualities of the consequent reconstructions. Optimizing the CBCT reconstruction processing chain for image quality was beyond the scope of this evaluation.

Simulations with 2.5 MV and 6 MV ran longer than that with 6 MV FFF at the same total dose. For 6 MV, more off-axis particles were delivered than 6 MV FFF to form a flat profile across the field, causing longer run time. For 2.5 MV, source particles had lower energy and, consequently, more particles were delivered to achieve the same dose at the calibration depth as a 6 MV FFF, causing longer run time as well.

4.4. Conclusion/Recommendation

A novel, FastEPID-based strategy for rapid MV-CBCT simulation was developed in this chapter. The run time of a 720-projection MV-CBCT simulation executed on a CPU cluster was shortened to a matter of hours without compromising the reconstruction quality. The proposed strategy can benefit development of novel flat panel detectors and clinical applications associated with MV-CBCT.

67

4.5. Reference

Bush K, Zavgorodni S F and Beckham W A 2007 Azimuthal particle redistribution for the reduction of latent phase-space variance in Monte Carlo simulations *Phys Med Biol* **52** 4345-60

Cheung J, Aubry J F, Yom S S, Gottschalk A R, Celi J C and Pouliot J 2009 Dose recalculation and the Dose-Guided Radiation Therapy (DGRT) process using megavoltage cone-beam CT *Int J Radiat Oncol Biol Phys* **74** 583-92

Feldkamp L A, Davis L and Kress J W 1984 Practical cone-beam algorithm *Josa a* **1** 612-9

Ferguson D, Shi M, Jacobson M, Myronakis M, Lehmann M, Huber P, Morf D, Fueglistaller R, Baturin P and Harris T *MEDICAL PHYSICS,2019),* vol. Series 46*)*: WILEY 111 RIVER ST, HOBOKEN 07030-5774, NJ USA) pp E334-E

Glover G H 1982 Compton scatter effects in CT reconstructions *Med Phys* **9** 860-7

Graham S A, Moseley D J, Siewerdsen J H and Jaffray D A 2007 Compensators for dose and scatter management in cone-beam computed tomography *Med Phys* **34** 2691-703

Hu Y, Baturin P, Wang A, Rottmann J, Myronakis M, Fueglistaller R, Huber P, Shi M, Shedlock D and Morf D *MEDICAL PHYSICS,2018),* vol. Series 45*)*: WILEY 111 RIVER ST, HOBOKEN 07030-5774, NJ USA) pp E461-E

Hu Y H, Shedlock D, Wang A, Rottmann J, Baturin P, Myronakis M, Huber P, Fueglistaller R, Shi M and Morf D 2019 Characterizing a novel scintillating glass for application to megavoltage cone‐beam computed tomography *Medical physics* **46** 1323-30

Lozano I V, Myronakis M, Shi M, Baturin P, Lehmann M, Fueglistaller R, Huber P, Morf D, Ferguson D and Harris T *MEDICAL PHYSICS,2019),* vol. Series 46*)*: WILEY 111 RIVER ST, HOBOKEN 07030-5774, NJ USA) pp E428-E

Parsons D, Robar J L and Sawkey D 2014 A Monte Carlo investigation of low-Z target image quality generated in a linear accelerator using Varian's VirtuaLinac *Med Phys* **41** 021719

Rottmann J, Morf D, Fueglistaller R, Zentai G, Star-Lack J and Berbeco R 2016 A novel EPID design for enhanced contrast and detective quantum efficiency *Phys Med Biol* **61** 6297-306

Shi M, Myronakis M E, Jacobson M W, Lehmann M, Ferguson D, Baturin P, Huber P, Fueglistaller R, Harris T, Valencia Lozano I, Williams C, Morf D and Berbeco R I 2020 A rapid, accurate image simulation strategy for mega-voltage cone-beam computed tomography *Phys Med Biol*

Townson R W, Jia X, Tian Z, Graves Y J, Zavgorodni S and Jiang S B 2013 GPU-based Monte Carlo radiotherapy dose calculation using phase-space sources *Phys Med Biol* **58** 4341-56

V. GPU-ACCELERATED MONTE CARLO SIMULATION OF MV-CBCT

In chapter 5, a GPU-based MC simulation framework integrated with the FastEPID technique for rapid, accurate simulation of MV-CBCT is proposed and validated. This simulation framework generates a series of phantom projections from a single simulation run. The time savings will accelerate the development of novel detectors and clinical applications associated with MV-CBCT that would otherwise be severely hampered by onerous simulation times.

This chapter is based on work submitted for publication: Shi M, Myronakis M, Jacobson M, Ferguson D, Williams C, Lehmann M, Baturin P, Huber P, Fueglistaller R, Valencia Lozano I, Harris T, Morf D and Berbeco R. GPU-accelerated Monte Carlo simulation of MV-CBCT. Submitted to *Phys Med Biol* (Shi M, 2020).

5.1. Method and materials

5.1.1. GPU thread assignment and simulation software

To obtain the best computational performance, a GPU thread often processes a fundamental data element. It can handle a single particle from its generation from beam source to the detection on imager, as well as an imager pixel for image generation. In the proposed strategy, the GPU threads are implemented in both ways. Running computation on millions of threads, a large number of particles can be processed simultaneously, as well as the imager pixels.

69

In this study, GATE version 7.2 and Geant4 v10.02 were compiled with CUDA 9.2 for the implementation of GPU-based MC simulation.

5.1.2. Overview of workflow and simulation environment
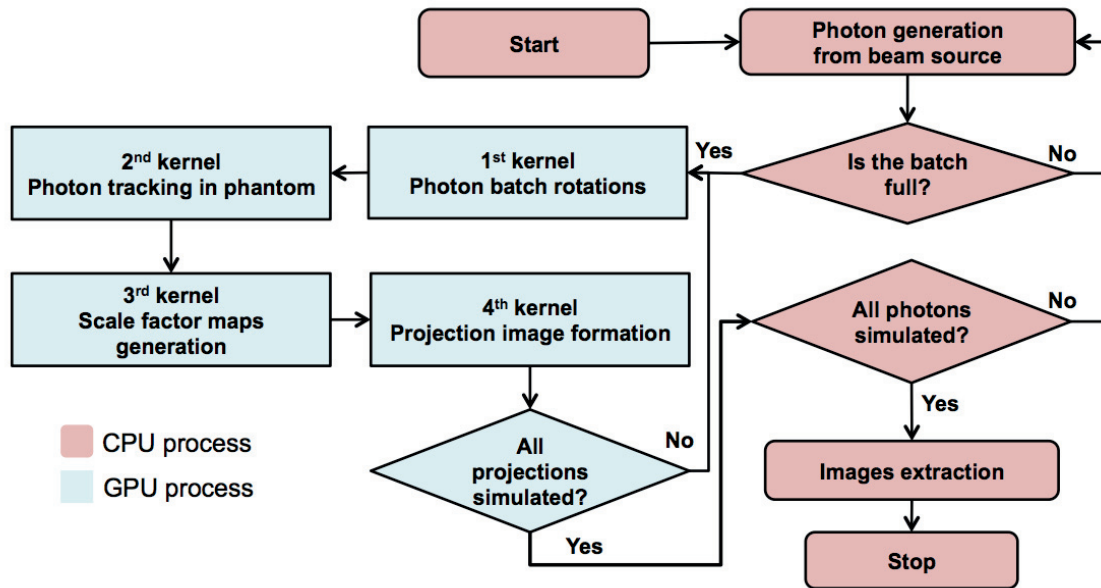
Figure 26 Workflow diagram of GPU accelerated MV-CBCT simulation.

As shown in Figure **26**, the MV-CBCT simulation framework consists of CPU processes and GPU processes. Starting with the CPU process, primary photons are emitted from the beam source towards a phantom volume. Photons entering the phantom surface are saved in a photon batch with a size adjusted according to the GPU global memory. Once the photon batch is full, it is copied to and saved on the GPU global memory. Four GPU kernels are executed in sequential order. Each of them represents a specific simulation process. The first kernel rotates the photon batch from the initial gantry angle to a given angle, kernel 2 simulates the photon transport through the phantom volume, kernel 3 determines the photon detection on the imager and computes data necessary for image formation, and kernel 4 generate a projection image. Kernels 1 to 4 are executed for each projection angle until all required projections are simulated.

70

Then, the simulation returns to the CPU process and repeats with another photon batch until all required primary photons are simulated. Projections at the same angle are accumulated and saved on CPU memory. Once all photons are simulated, these projections are extracted from the simulation and reconstructed to yield phantom volumetric images. A detailed description of each process can be found in Section 5.1.3.

5.1.3.   Detailed workflow

5.1.3.1.   CPU process: Photon generation

The primary photons are emitted from the beam source towards the phantom volume. The phantom volume is a voxelized volume extracted from a real diagnostic CT scan of the phantom. Photons entering the phantom surface are saved in a structure of arrays one after another. Each array within the structure saves the same sort of photon information and has a length that is equal to the batch size (Bert *et al.*, 2013). The information saved in the arrays is photon position, direction, energy, and associated simulation status. The photons are saved in the same order in all arrays. During the following processes, a GPU thread could collect information for a particular photon by accessing the same element index across these arrays. Once the batch is full, the CPU process is paused and the array structure is copied to the GPU global memory and used as the photon batch for the following simulation.

In the present study, the photon batch size was set to 50 million for a GPU card equipped with 8 GB global memory. Unlike a regular dose simulation that stops at a satisfactory uncertainty, an image simulation runs until the required dose, which is equivalent to the number of primary photons, is achieved. In this study, Varian TrueBeam phase space sources were used as the beam sources, and the equivalence between Linac

71

MU and the number of primary photons was derived from a calibration simulation described in Appendix.2. Generally, all the MV-CBCT projections are acquired at the same MU. The corresponding number of primary photons can be calculated as the product of the MU and the equivalence value. As the primary photon number is much greater than the batch size, multiple batches are generated for simulation.

5.1.3.2.   GPU kernel 1: Photon rotation about the phantom volume

Several simulation parameters are pre-defined by the user, including initial angle θ_{int}, angle increment $\Delta\theta$, and the number of projections. Angle of the ith projection θ_i is then computed by:

$$\theta_i = \theta_{int} + (i - 1) \times \Delta\theta \tag{16}$$

Since the characteristic of the beam source does not vary with gantry rotation, the same photon batch can be used for projection simulation at different angles. However, any fixed pattern noise of the photon batch would be retained in all projection images and lead to ring artifacts on the reconstructed images. To eliminate the fixed pattern noise, the batch photons need to be rotated arbitrarily about the beam central axis before rotating about the phantom.

The first kernel loads photons from the batch, rotates the photons about the beam central axis by an arbitrary angle, rotates the photons around the longitudinal axis of the phantom volume by θ_i, relocates them to the phantom surface, and writes the new photon state data back to the batch structure. Both the rotation and the relocation are computed analytically.

5.1.3.3.   GPU kernel 2: Photon tracking within the phantom volume

The GPU-based photon tracking package chosen for this study is a Geant4-based package introduced by Bert *et al.* (Bert *et al.*, 2013). The associated CUDA code is

72

incorporated within GATE and has been integrated into the proposed simulation strategy. Only a brief introduction of the chosen GPU tracking package is presented here. A detailed description can be found in Bert *et al.* (Bert *et al.*, 2013).

The main physical processes implemented in the GPU-based photon tracking algorithm are photoelectric effect and Compton scattering, provided by the Geant4 standard model. Computation of photon cross-sections, scattering angles, and energy loss are based on the interaction materials and photon energy. The associated CUDA code is translated from Geant4 without any approximations. The Woodcock tracking method is implemented for photon navigation in the phantom to avoid intensive computation. (Woodcock *et al.*, 1965). Electron transport in the phantom is not considered as they would be shielded by the imager copper buildup layer and would not contribute to the image. Bremsstrahlung x-rays generated from electron interactions are deemed negligible.

A Brent-XOR246s generator, featured by high periodicity, low memory requirement, and fast generation, is chosen as the random number generator in the GPU simulation (Brent, 2006). It can also execute independently on a GPU thread without communicating to other threads, allowing an easy implementation on the GPU architecture. A detailed description of the GPU-based Brent generator can be found in Bert *et al* (Bert *et al.*, 2013).

The second kernel of the proposed framework loads photons from the batch, transports each of them within the phantom volume forward by one step, update their simulation status, and writes their new state back to the batch structure. This kernel is repeated to move the photons forward step by step until they reach the phantom volume

73

boundary, or have energy lower than the user-defined energy cut, or get absorbed by the phantom materials. Photons reaching the phantom boundary with energy higher than the energy cut are kept active in the following simulation, while the others are killed by changing their simulation status to "false".

5.1.3.4.   GPU kernel 3: Photon detection and scale factor map generation

A conventional MC imager model is normally built by specifying the material composition and geometric arrangement of each component. By contrast, a virtual imager volume is modeled analytically with the same size and pixel pitch as the real EPID for the GPU simulation. The virtual imager is placed at a fixed SID and rotated simultaneously with the photon batch around the phantom volume through analytical computation.

The third kernel loads the active photons from the batch, calculates their incident positions on the virtual imager, determines photon detection using random numbers, and generates two scale factor maps (SFM). Since photon interaction with air is negligible for MV energy, the photon incident position is analytically computed from the photon position and direction relative to the imager model. Photons missing the virtual detector are terminated from subsequent simulation. A modified FastEPID technique is implemented to determine photon detection and generate SFMs, whose purpose is discussed next.

The regular FastEPID technique introduced in Section 3.1.1 works for photon simulation in sequential order and it is not readily transferrable to a GPU architecture. One problem is the interaction between threads when they are simultaneously adding OSFs to the EPID image. For instance, when two photons next to each other are detected, their OSFs would overlap on the EPID image, and one GPU thread has to wait until the

74

other one finishes writing to avoid any memory conflicts. Another problem is the pixel-by-pixel OSF addition operation, which results in too much memory access and long computation time. To mitigate these issues, a modified FastEPID technique is proposed by introducing two SFMs, as described below.

For each active photon with energy E incident on the virtual imager, A RN is generated, and a scale factor r and the corresponding η are calculated as follows:

$$r(E) = \frac{E - en\_low}{en\_high - en\_low} \tag{17}$$

$$\eta(E) = \left(1 - r(E)\right) \times \eta_{en\_low} + r(E) \times \eta_{en\_high} \tag{18}$$

Where, **en_low** and **en_high** refer to the lower and upper boundary of the corresponding energy bin, respectively. If the RN is less than or equal to $\eta(E)$, the photon is determined as "detected", and two SFMs are updated accordingly. SFM_r records the accumulated scale factors **r** for photons detected at a given pixel with a given energy bin, while SFM_N records the total number of photons detected at the same pixel within the same energy bin. Both SFMs are saved on the GPU global memory with a length of NX × NY × NE elements. "NX" and "NY refer to the number of pixels along the x and y dimensions of the imager, respectively. "NE" refers to the total number of energy bins. Each GPU thread would update one element of the SFMs at a time, allowing only two memory access operations for a detected photon. This method would save a great deal of time compared to the 81 × 81 access operations using the regular FastEPID method. The SFMs are updated using atomic writes to keep synchronization among threads.

To further accelerate the simulation, the η values are scaled up by a factor of $1/((\text{maximum } \eta))$ to reduce the number of primary photons required for simulation. This

method is capable of shortening the simulation time by the same scale factor without compromising the qualities of the projection and reconstructed images. Validation studies were performed using the AS1200 imager and two phantoms, Las Vegas phantom and Catphan 604 phantom. The results are presented in Appendix 4.

5.1.3.5.   GPU kernel 4: EPID image generation

Since the modified FastEPID technique is implemented, the EPID image is no longer generated from the accumulation of OSFs. Instead, it is generated from the pre-calculated OSFs and SFMs. OSF centered at a given image pixel (i, j) are scaled by the SFM_r and SFM_N at the same pixel for a given energy bin E, using:

$$OSF(E) = (SFM\_N(E) - SFM\_r(E)) \times OSF_{en\_low} + SFM\_r(E) \times OSF_{en\_high} \quad (19)$$

Then, the summation of the OSFs centered at the same pixel through all energy bins is added to the EPID image with the center aligned to pixel (i, j).

In GPU kernel 4, a single GPU thread handles an element of the total OSF that would be added to the EPID image centered at a given image pixel. For example, in the case of a 8×8 pixels imager updating with 3×3 elements OSFs shown in Figure **27**, GPU threads 1-9 handle the total OSF that would be added to pixel (1, 1), and threads 64-72 handle the OSF for pixel (8, 1), etc. The number of threads needed for this imager is equal to $8 \times 8 \times 3 \times 3$. In the case of the AS1200 imager, a total number of $1.07495424 \times 10^{10}$ threads (= $1280 \times 1280 \times 81 \times 81$) are required to generate the image. The forth kernel assigns a GPU thread with OSF indices and imager indices, calculates the total OSF value following Equation 19, and updates the EPID image using atomic write operation. Finally, the EPID image is added to the accumulated image generated with previous batches and copies to the host CPU memory.
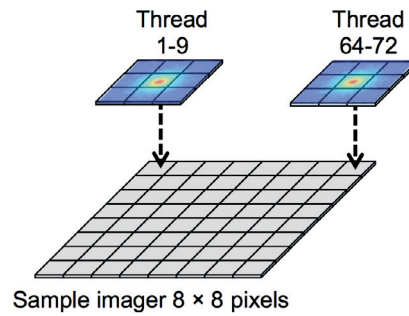
76

Sample imager 8 × 8 pixels

Figure 27 Example of an imager with 8 × 8 pixels updated by OSFs with 3 × 3 elements.

5.1.4. GPU implementation and hardware

The GPU-based hardware consisted of a CPU host (Intel® Xeon® Gold 6130 CPU @ 2.10 GHz with 192 GB RAM) and a GPU device (NVIDIA Tesla V100 card with 5120 CUDA cores). The GPU block size was set to 1024 for all kernels, and the grid size was calculated from either the batch size (kernel 1 to 3) or the total number of threads needed for image formation (kernel 4).

5.1.5. Validation studies

The proposed GPU-based MV-CBCT simulation was validated against measurement and CPU-based implementation of FastEPID using a Catphan 604 phantom and a pelvis phantom. Each phantom was scanned with the Varian AS1200 imager on a Varian TrueBeam Linac at beam energies of 2.5 MV, 6 MV, and 6 MV FFF. MV-CBCT images were reconstructed using the FDK algorithm. Comparison of the MV-CBCT images was performed and the improvement in run time was evaluated with the GPU- and CPU-based simulations.

5.1.5.1.   Beam sources, phantoms, image generation, and MV-CBCT acquisition

Varian TrueBeam phase space sources were utilized as the source inputs in both CPU-based and GPU-based simulations due to their ability to provide accurate source characterization (Townson *et al.*, 2013). A detailed description of the source can be found in Section 4.1.1.1 and Appendix.2.

Digital versions of the phantoms were derived from the corresponding diagnostic CT scans. The CT numbers were segmented into different materials with a user-defined density conversion table. Detailed descriptions of the phantoms and the properties required for phantom modeling can be found in Section 4.1.1.

The CPU-based simulated images were generated utilizing the original FastEPID method introduced in Section 3.1.1, while the GPU-based ones were generated with the modified FastEPID method described in Section 5.1.3. MV-CBCT acquisition and reconstruction followed the same setup and processes described in Section 4.1.1.3 and Section 4.1.1.4, respectively.

5.1.5.2.　　　　Catphan 604 and pelvis phantom validation studies

To evaluate the ability of the proposed GPU-based simulation to reproduce scatter and beam hardening effects, the cupping artifact was evaluated following the method introduced in Section 4.1.2. The mean HU and contrast-to-noise ratio (CNR) of the phantom inserts were evaluated and compared between measurement and simulation following the method introduced in Section 4.1.2. The reconstructions of the pelvis phantom were compared in terms of the overall image performance, the mean HU, and the standard deviation following the method introduced in Section 4.1.2.

5.1.5.3.　　　　Run time of the GPU-based and CPU-based MV-CBCT simulations

78

The GPU-based simulation was executed on several NVIDIA Tesla V100 GPU cards, while the CPU-based simulation was executed on a high performance computing CPU cluster. To offer a fair comparison, the run time was evaluated in GPU hours and CPU hours. It was also normalized to 1 MU for the comparison between beam energies. Run time of the CPU-based simulation was scaled to the dominant CPU model equipped on the cluster, AMD Opteron™ Processor 6380 2.5 GHz. The time improvement was computed as the ratio of the CPU-based simulation time to the GPU-based simulation time.

5.2.   Results

5.2.1. Catphan 604 phantom validation study

The reconstruction images of the Catphan urethane slab are displayed and compared in Figure **28**. The agreement in image quality between measurement and simulations is excellent. The quantitative cupping artifact values and the diff% from the GPU-based simulation are listed in Table **16**. Less than 3% difference is observed, indicating that the cupping artifact captured by the GPU simulation was similar to that of the measurement and the CPU-based simulation.

Table 16 The cupping artifact captured by measurement and simulations. Percentage difference listed in parentheses is the difference from the GPU-based simulation.

Beam energy	2.5 MV	6 MV	6 MV FFF
Measurement	0.843 (1.74%)	0.736 (1.18%)	0.817 (2.08%)
CPU simulation	0.851 (2.69%)	0.749 (0.46%)	0.828 (0.77%)
GPU simulation	0.829	0.745	0.834

79
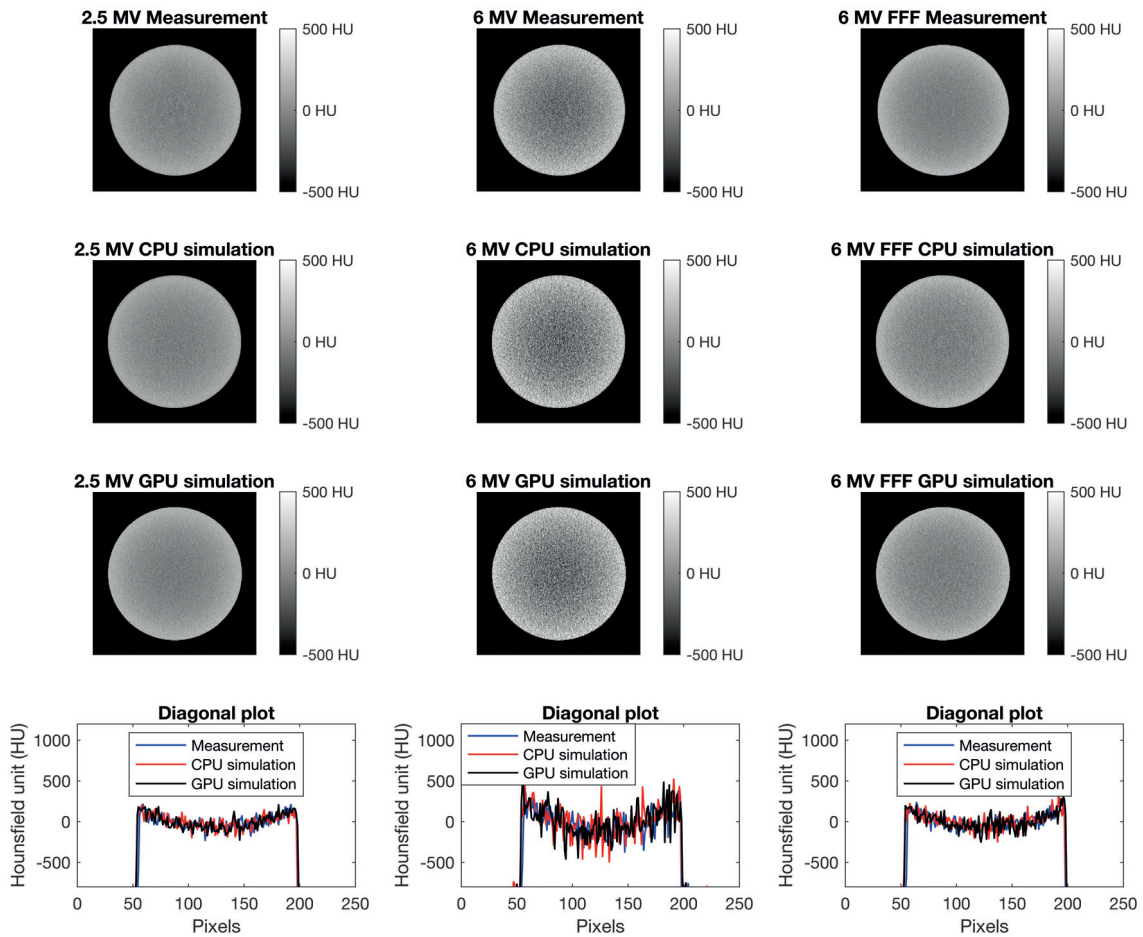
Figure 28 Reconstructed images of the Catphan (urethane slab slice) and the diagonal profiles.

The reconstruction results of the Catphan 604 phantom are displayed in Figure **29**, Figure **30**, and Figure **31**, for sample images, HU plot, and CNR plot, respectively. The agreement between measurement and simulations are excellent in terms of the image quality, mean HU, and CNR for all beam energies.
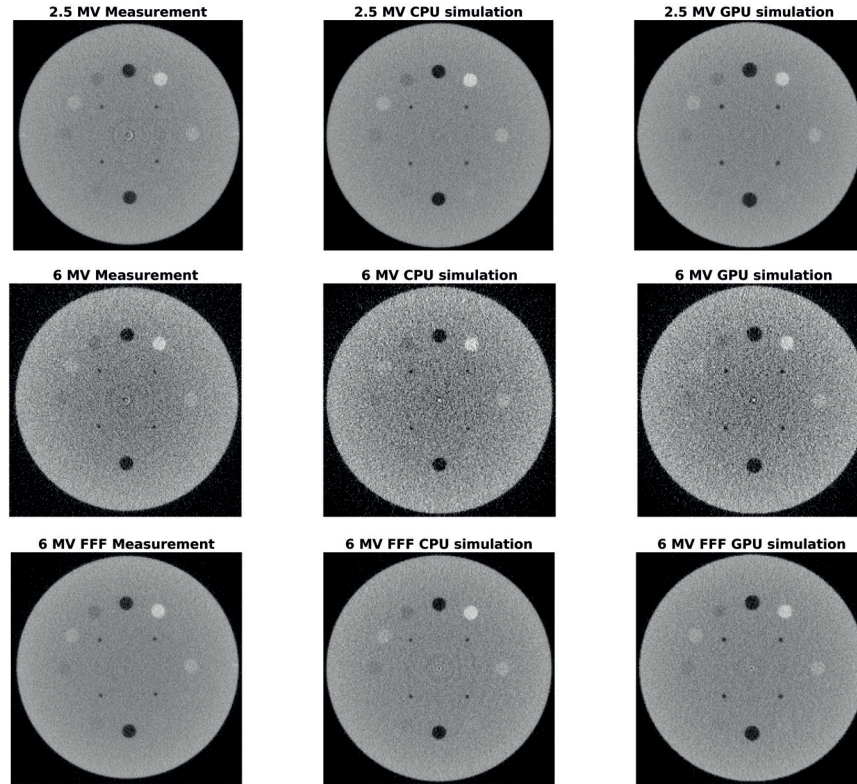
Figure 29 The reconstruction images of Catphan 604 phantom.
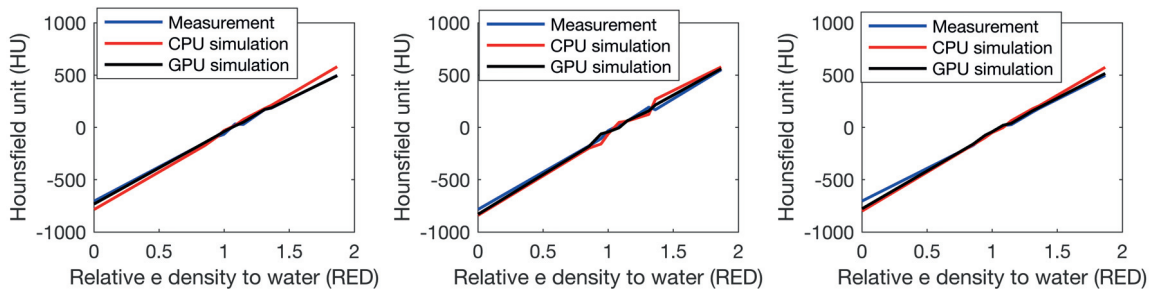
Figure 30 The mean HU of Catphan 604 phantom inserts.
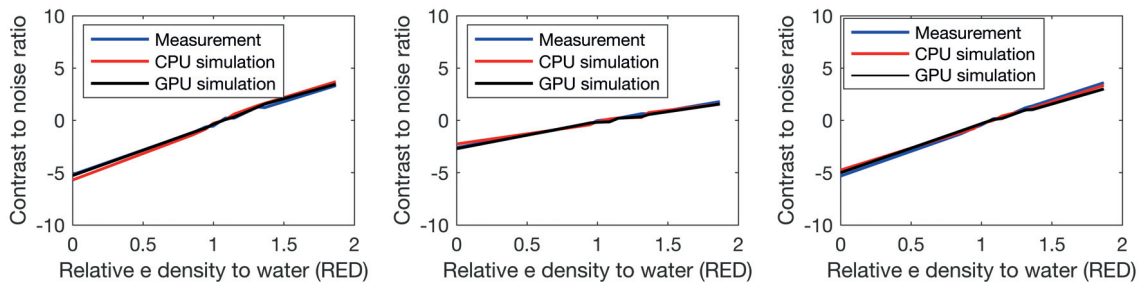
Figure 31 The CNR of Catphan 604 phantom inserts.

5.2.2. Pelvis phantom validation study

The reconstruction images of the pelvis phantom containing the same bone structure are displayed in Figure **32**. Similar image performance is observed between measurement and simulations. Mean HU and the standard deviation of the ROIs are listed in Table **17**. The good agreement between measurement and simulations indicates that image signal and noise is well simulated with the proposed GPU approach.
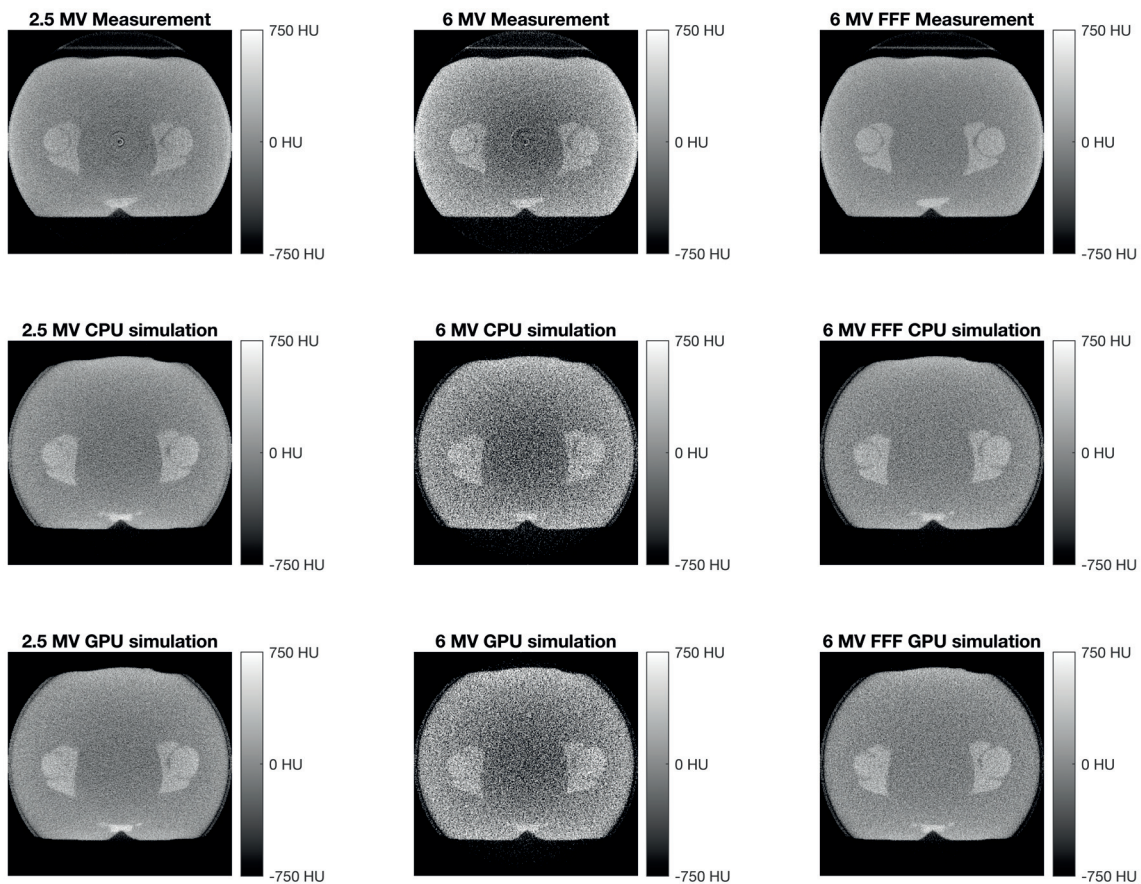
Figure 32 The reconstruction images of the pelvis phantom.

Table 17. Comparison of mean HU and standard deviation of the pelvis phantom.

Soft tissue			
Beam energy	Image acquisition	Mean HU	Standard deviation (HU)
	Measurement	5.3	115.4
2.5 MV	CPU simulation	-3.3	122.1
	GPU simulation	-1.4	136.0
	Measurement	-3.6	234.9
6 MV	CPU simulation	-12.0	290.9
	GPU simulation	27.3	358.0
	Measurement	-4.2	107.9
6 MV FFF	CPU simulation	-4.4	134.5
	GPU simulation	-2.9	153.1
Bone			
Beam energy	Image acquisition	Mean HU	Standard deviation (HU)
	Measurement	124.9	142.5
2.5 MV	CPU simulation	166.8	141.9
	GPU simulation	161.1	136.2
	Measurement	203.0	256.4
6 MV	CPU simulation	233.9	334.8
	GPU simulation	199.5	327.0
	Measurement	189.4	128.0
6 MV FFF	CPU simulation	210.1	163.2
	GPU simulation	195.4	155.5

83

5.2.3. Run time of the GPU-based and CPU-based MV-CBCT simulation

Run time of the MV-CBCT simulation utilizing the CPU-based and GPU-based simulations and the corresponding time improvement are listed in <u>Table **18**</u>. The GPU-based simulation has shortened the run time by a factor up to 2300, depending on the beam energy and the phantom volume.

<u>Table 18 Run time of MV-CBCT simulations (normalized to 1 MU).</u>

Beam energy	Catphan 604		
	CPU hours	GPU hours	Improvement
2.5 MV	94800	103.5	916
6 MV	107400	55.8	1924
6 MV FFF	57000	39.6	1439
Beam energy	Pelvis phantom		
	CPU hours	GPU hours	Improvement
2.5 MV	156000	96.3	1620
6 MV	128400	56.8	2260
6 MV FFF	95700	40.5	2363

5.3. Discussion

The excellent time improvement realized with the proposed GPU-based framework for MV-CBCT simulation was related to three major factors. The first one was the re-use of the photon batch for simulating projections at different angles. According to a test run where only one projection image was generated using the proposed GPU strategy, 75% of the run time was spent on the CPU process, and the remaining 25% was spent on the GPU process. It means that the photon generation is a time-consuming process and

84

should be executed as less frequently as possible. By rotating the photon batch around the phantom, the primary photons were generated once but reused for all projections. It effectively reduced the CPU time while kept the GPU time the same. It was found that only 3% of the time was spent on the CPU and the remaining 97% was spent on the GPU for a 720-projection MV-CBCT simulation.

Secondly, the integrated FastEPID method has provided a solution for the parallel simulation of EPID image. Essentially, the FastEPID method is a table-lookup method. It can be easily implemented in a GPU environment with a slight modification. Conversely, parallelizing a direct MC simulation of EPID is impractical due to the high computational demands of simulating optical photon transport. In reality, the optical photons are generated from scintillation events trigged by x-ray photon energy deposition in the phosphor layer. Each scintillation event yields thousands of optical photons at one MeV energy deposition. In order to track all the optical photons, too much GPU memory would be occupied, resulting in a limited batch size and a large number of photon batches, further causing longer simulation time.

The third factor was the adoption of the GPU-based photon tracking package, introduced by Bert *et al.* (Bert *et al.*, 2013). This package enables the parallel simulation of photon transport through phantom volume and has time improvements of 400- to 800-fold depending on the simulation subject. Other factors such as the implementation of the scaled η values and the powerful GPU hardware also contributed to the time improvement.

The proposed GPU-based strategy takes into account photon transport within the imager by implementing the modified FastEPID method. It allows a direct comparison

85

between our GPU simulation and measurement in terms of image signal and noise, both of which are critical for MV-CBCT image evaluation and MV imager optimization. In contrast, previous studies simplified the imager response by deriving pixel values from energy deposition or counting photons reaching the imager (Bert *et al.*, 2013; Jia *et al.*, 2012), both of which would not replicate the signal and noise as accurately. To the best of our knowledge, the proposed GPU-based strategy is the first published study to include simulations in both phantom and imager that provide signal and noise information comparable to experimentally acquired results.

5.4. Conclusion/Recommendation

A GPU-based strategy suitable for MV-CBCT simulation was developed based on a customized simulation framework and a modified FastEPID technique. Two phantoms were simulation for validation at multiple beam energies. Comparisons were made between reconstructions of measurement and simulations. No difference in visual image quality was observed and close agreement between quantitative image quality measures were realized. Speed-up factors up to 2300 were achieved by the implementation on a GPU architecture. The proposed GPU strategy can benefit MV imager optimization and clinical studies related to MV-CBCT.

5.5. Reference

Bert J, Perez-Ponce H, El Bitar Z, Jan S, Boursier Y, Vintache D, Bonissent A, Morel C, Brasse D and Visvikis D 2013 Geant4-based Monte Carlo simulations on GPU for medical applications *Phys Med Biol* **58** 5593-611

Brent R P 2006 Some long-period random number generators using shifts and xors *ANZIAM Journal* **48** 188-202

Jia X, Yan H, Cervino L, Folkerts M and Jiang S B 2012 A GPU tool for efficient, accurate, and realistic simulation of cone beam CT projections *Med Phys* **39** 7368-78

Shi M M M, Jacobson M, Ferguson D, Williams C, Lehmann M, Baturin P, Huber P, Fueglistaller R, Valencia Lozano I, Harris T, Morf D and Berbeco R 2020 GPU-accelerated Monte Carlo simulation of MV-CBCT *Submitted to Phys Med Biol*

Townson R W, Jia X, Tian Z, Graves Y J, Zavgorodni S and Jiang S B 2013 GPU-based Monte Carlo radiotherapy dose calculation using phase-space sources *Phys Med Biol* **58** 4341-56

Woodcock E, Murphy T, Hemmings P and Longworth S *Proc. Conf. Applications of Computing Methods to Reactor Problems,1965),* vol. Series 557*)*

VI.   CONCLUSION

This dissertation has mainly focused on the development of a GPU-accelerated strategy of MV-CBCT simulation based on the FastEPID technique and a customized simulation framework. With the proposed strategy, the simulation of a full MV-CBCT scan can accomplish within hours rather than weeks or months, allowing its usage in imager optimization and MV-CBCT related clinical studies. We recommend further studies on the improvement of the FastEPID method and the proposed GPU simulation strategy, as well as the development towards clinical applications.

EPID image simulation has been accelerated tremendously by utilizing the FastEPID method. The photon detection is determined through a binary sampling process and the imager response is replaced by pre-calculated OSFs. However, there is room for improvement. Firstly, the photon detection is simplified as a perpendicular entrance at the center of the considered pixel without consideration of incident angle or off-center position. By carefully integrating additional sampling processes to determine the incident angle and position might help improvement the image quality while maintaining the same simulation speed. Secondly, the pre-calculated OSF is generated with a mono-energetic pencil beam consisting of 10^7 primary photons. It contains the noise feature representing the case of 10^7 photons incident at a given pixel for a given energy bin, which is much larger than that occurs in reality. Such an overestimation of incident photons leads to an underestimation in noise. A potential solution is to introduce an OSF-sampling process. For example, a few OSFs are pre-calculated with different number of primary x-rays for each energy bin. During the simulation, the number of incident photons N_{inci} is recorded

88

at each image pixel for each energy bin, and then the final EPID image is generated with the OSFs that are sampled based on N_{inci}.

Various parameters such as GPU block size and photon batch size can be optimized for future improvement. A typical GPU computation issue, thread divergence, existed in the phantom simulation. Common solutions to this problem like sorting photons by position and energy were not considered due to a concern of extra time spent on the sorting process. Time improvement will be expected in the future if more parameters are optimized as well as the thread divergence problem is solved.

A user-friendly interface is necessary for a broad implementation of the proposed simulation strategy. Currently, both the CPU and GPU processes run with GATE software, which requires certain knowledge for installation and programming. A stand-alone simulation code using C/C++ language can be more convenient to users without background in MC simulation.

Besides imager optimization, other MV-CBCT associated studies can benefit from the proposed simulation strategy. A large number of phantom projections under different conditions can be generated for the study of new reconstruction algorithms. KV-CBCT can be integrated into the proposed framework for the development of kV-MV scan time reduction technique and kV-MV CBCT field of view enlargement technique. Meanwhile, additional GPU kernel recording dose deposition in the phantom can be merged into the framework for image dose evaluation. Similarly, another GPU kernel simulating multi-leaf collimations can be added to generate beam-eye view projections for the development of real-time tracking algorithm.

VII.   APPENDIX

Appendix.1   A source model of Linac 6 MV beam: multi-point source

TrueBeam Linac phase-space files are generated above the secondary collimators by recording particles emerging from the treatment head. The recorded particle properties include energy, particle type, position, and direction. The broad use of the phase-space files as a simulation source has hindered by several intrinsic shortcomings. For example, approximately 3×10^8 particles are recorded in Varian TrueBeam 6 MV phase-space files, but more than 10^{11} primary particles are required to simulate a 0.1 MU EPID image. Recycling the phase-space files by random rotation can solve this problem, but introduce insufficient photon influence at the corner of a field size larger than 30×30 cm^2. Additionally, most particles are blocked by the secondary collimators when simulating a small field size, causing a tremendous waste of time.

In this study, we have modeled the Varian TrueBeam 6 MV phase-space files with a multi-point source. The source is an accumulation of point sources located at the same position 100 cm away from the iso-center, and each point source generates x-ray photons within a given solid angle that projects in a 0.5 cm width ring at the iso-center plane. An example showing a multi-point source formed by four point sources is shown in Figure **33**. Relative intensity and photon spectrum of each point source are extracted from the phase-space files. The number of point sources is determined in a way that the accumulated solid angle is sufficient to cover the required field size. For instance, 17, 31, 45, and 59 point sources are required to form 10×10 cm^2, 20×20 cm^2, 30×30 cm^2, and

90

$40 \times 40 \text{ cm}^2$ field sizes, respectively. Some of the ring areas are cut by the edge of the square field size, thus the relative intensity is modified based on the area loss.
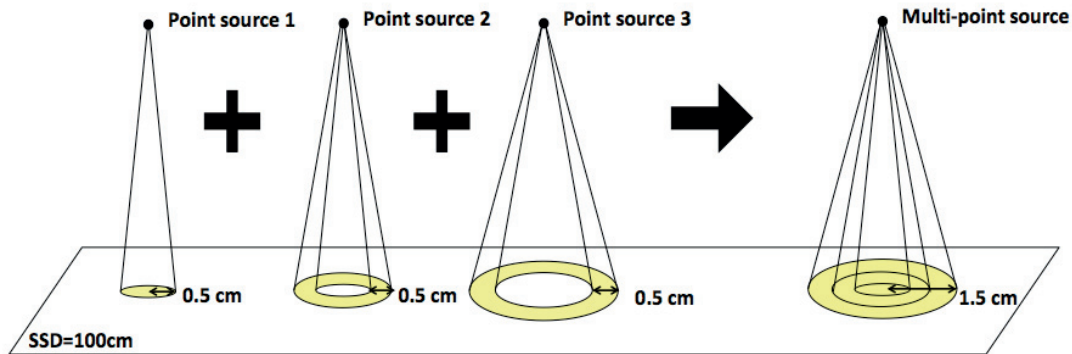

Figure 33 Illustration of multi-point sources created by overlaying three single point sources.

To model the Linac treatment beam, the multi-point source is placed appropriately, and each of point sources emits primary photons within the pre-defined solid angle following the corresponding energy spectrum and relative intensity. The secondary collimators are modeled to simulate the field size.

The multi-point sources for field sizes $10 \times 10 \text{ cm}^2$ to $40 \times 40 \text{ cm}^2$ were validated against experimental measurement and simulation using phase-space source in terms of percentage depth dose (PDD), relative dose profile, and output factor (OF). PDD measurement was performed in a water tank with SSD = 98.5 cm. The clinical Linac used in this study was calibrated to 1 MU/cGy at d_{max} (1.5 cm) with a $10 \times 10 \text{ cm}^2$ field size at SSD = 98.5 cm. Relative dose profiles were measured at d_{max} at SSD = 100 cm. The output factors were measured a 10 cm depth with SSD = 95 cm. Simulations were configured in the same way as the measurements. For the OF comparison, $4 \times 4 \text{ cm}^2$ and $15 \times 15 \text{ cm}^2$ field sizes were also included. The validation was quantified by the difference between measured and multi-point source simulated results.

Excellent agreement was found for PDD, relative dose profile, and OF comparisons, as shown in Figure **34**, Figure **35**, and <u>Table **19**</u>, respectively. PDD curves are scaled by different factors for better visualization. In general, the PDD curves agree well between measurement and multi-point source simulation, within 2% difference. A 3%-5% difference is observed at surface depths because electrons are not modeled in the multi-point source. This omission will not impact image simulation as the electrons are shielded by the EPID copper layer. The relative dose profiles match well between measurement and the multi-point source for all field sizes. A difference is observed at the field edge, which can be caused by the uncertainty in secondary collimator modeling. The OF agreement is good with negligible difference between the measurement and multi-point source simulation.

<u>Table 19 Output factor with different field sizes.</u>

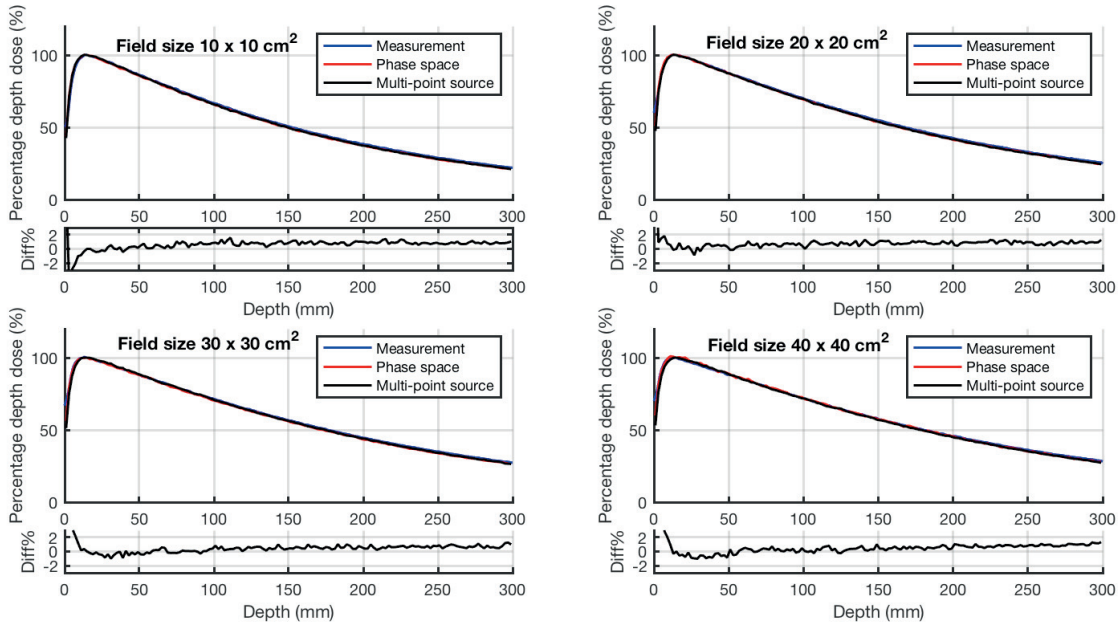| Field size	Measurement	Phase space simulation	Multi-point source
4×4 cm^2	0.9059	0.9033	0.9046
10×10 cm^2	1	1	1
15×15 cm^2	1.0410	1.0322	1.0328
20×20 cm^2	1.0708	1.0674	1.0699
30×30 cm^2	1.1110	1.1053	1.1059
40×40 cm^2	1.1160	1.1112	1.1192

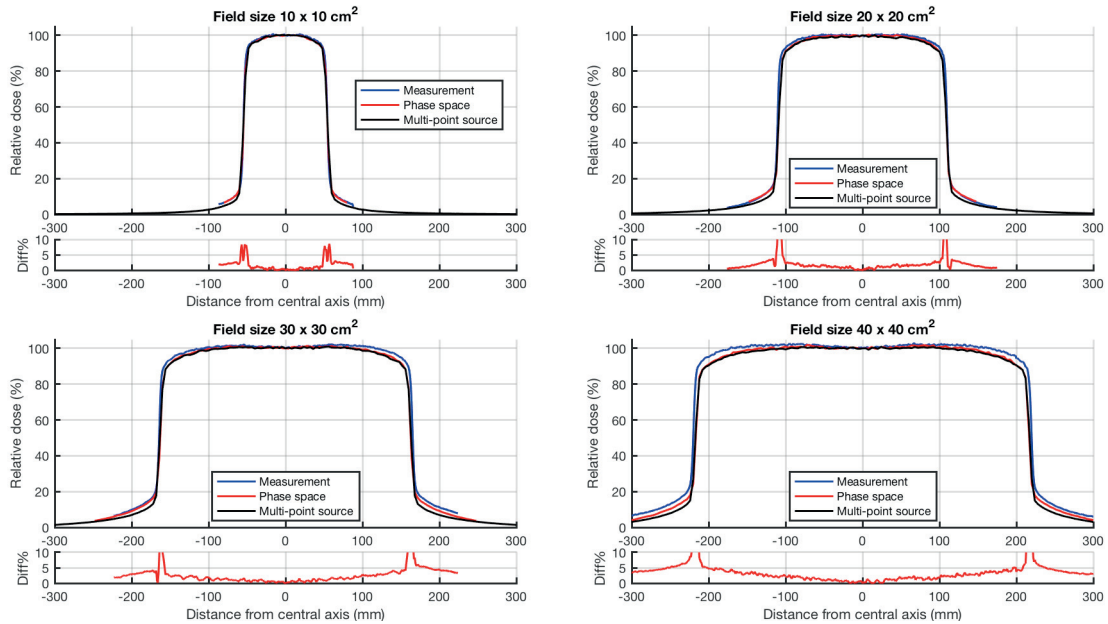Figure 34 The measured PDD, the simulated PDD, and the PDD difference.

Figure 35 The measured and simulated relative dose profiles, and the profile difference.

In summary, the proposed multi-point source can replace Linac phase-space files and be used to as the source model in simulation. This source saves all the beam information in a simple data file and can be sampled repeatedly without any concerns on running out of particles.

93

Appendix.2   Validation of the Varian phase space sources

Simulation using the Varian TrueBeam phase space sources of 2.5 MV, 6 MV, and
6 MV FFF were validated against measurement in terms of PDD, relative dose profile,
and OF. File specifications of the phase space sources are listed in <u>Table **20**</u>.

<u>Table 20 Parameters of Varian TrueBeam phase space files.</u>

Beam energy	File number	File size (MB)	Number of particles saved in files (millions)
2.5 MV	15	~ 600	330
6 MV	6	~ 1800	310
6 MV FFF	10	~ 1100	470

PDD curves and relative dose profiles were measured in a water tank at SSD = 100
cm with field size 10×10 cm^2, 20×20 cm^2, 30×30 cm^2, and 40×40 cm^2. Relative dose
profiles were recorded at 5 cm depth for 2.5 MV and at 1.5 cm depth for 6 MV and 6 MV
FFF, and they were normalized to the central axis dose. The output factor of 30×30 cm^2
field size was calculated at 5 cm depth at SSD = 95 cm. MC simulations utilizing the
phase space sources were performed with the same setup. The validation was quantified
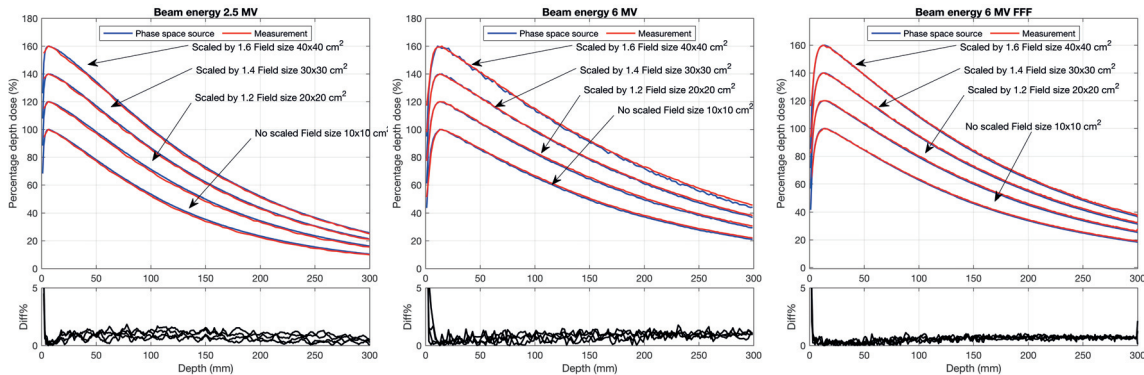by the agreement between measurement and phase space based simulation.

Figure 36 The measured PDD, the simulated PDD, and the PDD difference.

94

The PDD curves and relative dose profiles are illustrated in Figure **36** and Figure **37**. The PDD curves of different field sizes are distinguished by scaling with different factors for better visualization. Great agreement between measurement and simulation is observed for PDDs and relative dose profiles. A relatively large difference at the field edge for the relative dose profile comparison could be caused by the modeling uncertainty of the secondary collimators. As shown in Table **21**, OFs at 30×30 cm^2 match well between measurement and simulation. In summary, the phase space source can be used as an accurate source model of Varian TrueBeam Linac.
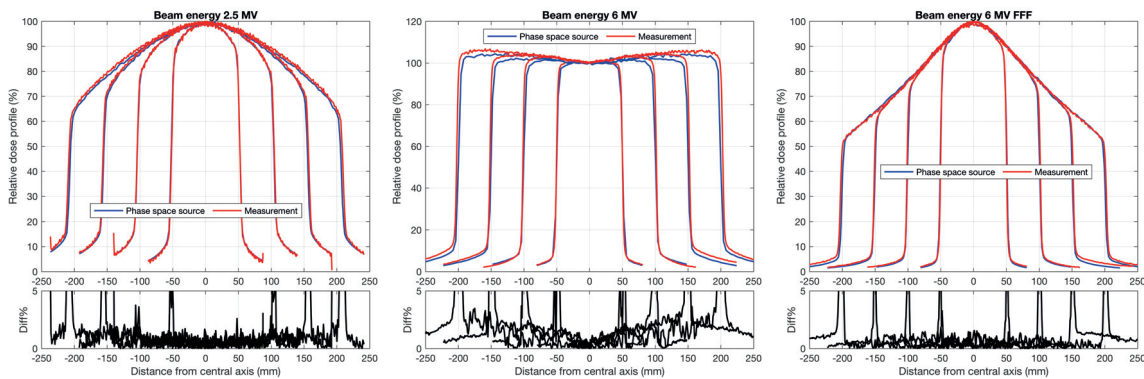

Figure 37 The measured and simulated relative dose profiles, and the profile difference.

The equivalence between the number of primary particles simulated and the Linac MU was established for a fair comparison between measurement and simulation in terms of imaging dose. The Linac beam used in this study was calibrated to deliver 1 cGy/MU to water at d$_{max}$ with SAD = 100 cm and 10×10 cm^2 field size. A calibration simulation was performed with the same setup. According to the simulation results, 1 cGy was deposited to d$_{max}$ by 5.34×10^{12}, 3.67×10^{12}, and 2.29×10^{12} particles generated from 2.5 MV, 6 MV, and 6 MV FFF phase space sources. For image dose other than 1 MU, the number of simulated particles was scaled accordingly.

Table 21 Output factors at 30×30 cm^2 field size. Percentage difference listed in parentheses is the difference from measurement.

	2.5 MV	6 MV	6 MV FFF
Measurement	1.1679	1.1109	1.0795
Phase space simulation	1.1412 (2.3%)	1.1053 (0.5%)	1.0700 (0.9%)

96

Appendix.3   Impact of CPU model on the FastEPID simulation time

The CPU models equipped in the high performance computing cluster provided different computation speeds based on processor specifications like processor base frequency, number of cores, memory size, and memory speed. Identical simulation jobs were randomly submitted to different CPU models, resulting in a distribution of job run time. The dominant CPU models are Intel® Xeon® Gold 6140 processor and AMD Opteron™ processor 6380. Jobs performed on Intel® Xeon® 6140 are completed much more quickly than those performed on AMD Opteron™ 6380.

Run time of the MV-CBCT simulations was evaluated with the less powerful CPU, AMD Opteron™ processor 6380, in Section 4.2.3. It can be re-evaluated with the more powerful CPU, Intel® Xeon® Gold 6140, to better understand the strength of the FastEPID method. As shown in Table **22**, the MV-CBCT simulations run on a Intel® Xeon® Gold 6140 CPU cluster takes less than 20 hours, much faster than if run on an AMD Opteron™ processor 6380 CPU cluster.

Table 22 Run time in hours of MV-CBCT simulation (normalized to 1 MU) performed on Intel® Xeon® Gold 6140 CPU cluster.

Beam energy	2.5 MV	6 MV	6 MV FFF
Catphan 604 phantom	9.0	10.2	5.4
Pelvis phantom	18.8	15.3	10.8

97

Appendix.4   FastEPID method with scaled energy deposition efficiency

During the regular FastEPID simulation, photon detection is determined when a newly generated RN is less or equal to η(E). Therefore, η(E) is equal to the detection probability of photons at energy E, and 1-η(E) is equal to the probability of photon penetration. In case of AS1200 imager (Figure **38**, left plot), the maximum η occurs at 90 keV with a value of 0.2067, meaning that 20.67% of the photons at this energy are detected and the rest penetrates through the detector without any contribution to the image.
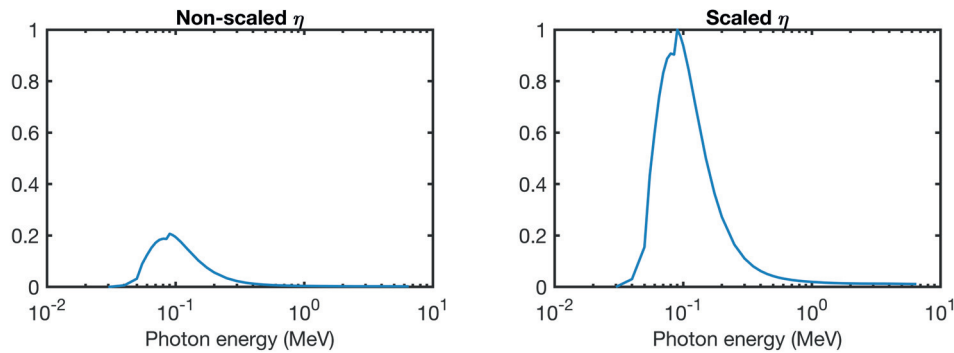

Figure 38 Photon energy deposition efficiency η of Varian AS1200 imager.

One way to accelerate the FastEPID simulation is to scale up the η values by a given factor and simultaneously scale down the number of primary photons by the same amount, resulting in the same number of detected photons. Since the simulation time is roughly proportional to the number of primary photons, it is reduced by that scale factor. The largest scale factor achievable is 1/(maximum η), which normalizes all η values to a maximum of one. For the case of the Varian AS1200 imager, the largest scale factor is 4.837, giving 100% photon detection at 90 keV. The scaled η values are plotted in Figure **38** (right plot). Since this method is a pure computational improvement and has no dependence on the hardware platform, it can be implemented in both the CPU-and GPU-

based FastEPID simulations. The validation study was performed by a comparison of image quality between simulations utilizing the regular and scaled η values. Planar images of the LV phantom and MV-CBCT reconstruction images of the Catphan 604 phantom were acquired and compared.

Planar images of the LV phantom were FastEPID simulated at 1 MU with both regular and scaled η values on a CPU cluster. The FastEPID virtual detector was placed at SID =153.5 cm while the phantom was placed at a SSD =100 cm. Phantom images were acquired with 15×15 cm^2 field size at beam energy 6 MV. The simulated phantom images are shown in Figure **39**. The overall image quality agrees well between the two simulations. Image profiles along the horizontal and vertical directions agree well. 99.7% and 100% of the image pixels had a less than 2% difference and less than 3% difference in the pixel value, respectively. A great agreement between the regular efficiency simulation and the scaled efficiency simulation was realized.
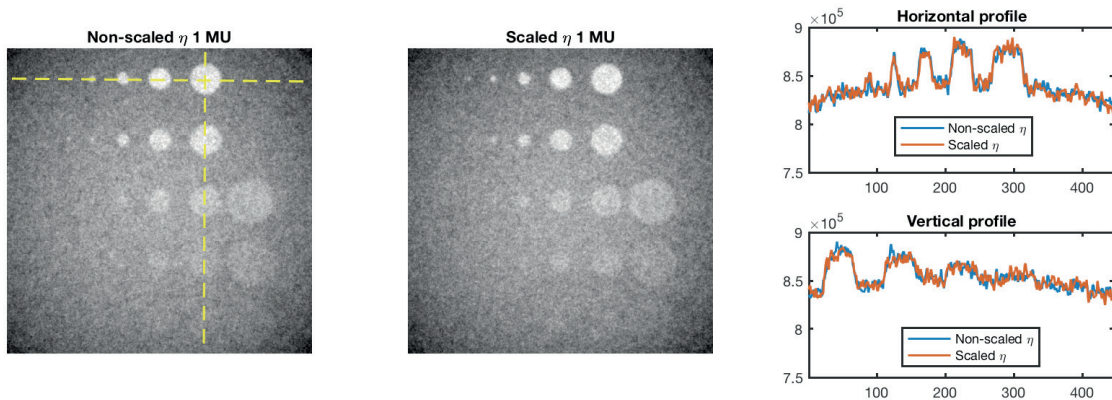

Figure 39 Las Vegas phantom images and the image profiles along the dash line.

The MV-CBCT simulation of Catphan 604 phantom at 2.5 MV beam energy was performed with the regular η values utilizing the GPU-based simulation strategy and the acquisition parameters listed in Section 5.1.5. The reconstructed images are displayed and

99

compared in Figure **40**. Great agreement between simulations is observed from the overall performance of the reconstructed phantom images. Image profiles along the horizontal and vertical directions agree well.
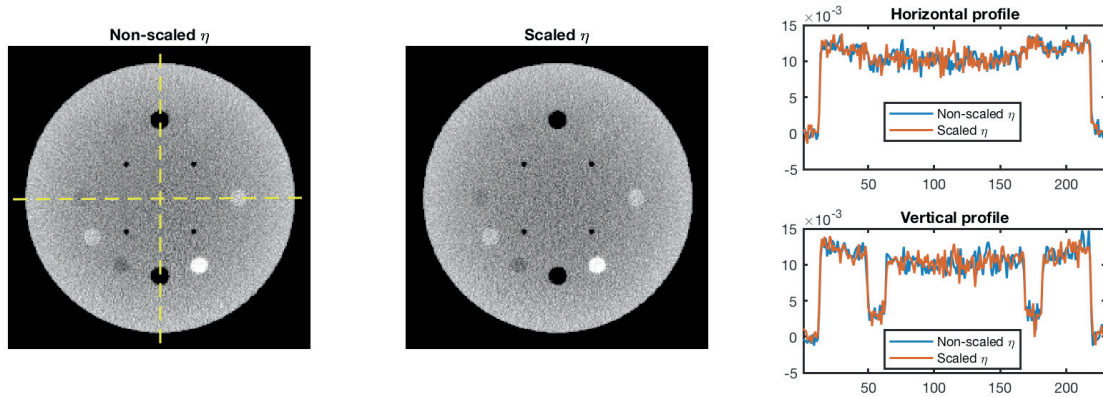

Figure 40 The reconstructed Catphan 604 phantom images and the image profiles along the dash line.